Water Resources Research

RESEARCH ARTICLE
10.1029/2024WR039579

Multi-Elevation UAV-Based Frequency Domain Electromagnetic Method for Data Calibration and Field Investigation

Qinbo Cheng[1], Zhijin Ma[2], Andrew Binley[3], Jiayun Chai[1], Jintao Liu[1,4], Zhicai Zhang[1], and Xi Chen[5]

[1]College of Hydrology and Water Resources, Hohai University, Nanjing, China, [2]Yellow River Institute of Hydrology and Water Resources, Zhengzhou, China, [3]Lancaster Environment Centre, Lancaster University, Lancaster, UK, [4]National Key Laboratory of Water Disaster Prevention, Hohai University, Nanjing, China, [5]School of Earth System Science, Tianjin University, Tianjin, China

Key Points:

- An UAV-FDEM method, designed to conduct surveys at specific flight heights along planned routes, is introduced to improve work efficiency
- A multi-elevation UAV-FDEM survey method is proposed that clearly reduces the inversion uncertainty compared to the single-elevation method
- A new calibration method for multi-coil FDEM, leveraging the multi-elevation UAV-FDEM in point measurement mode, is proposed

Supporting Information:

Supporting Information may be found in the online version of this article.

Correspondence to:

Q. Cheng,
Qinbo.Cheng@hhu.edu.cn

Citation:

Cheng, Q., Ma, Z., Binley, A., Chai, J., Liu, J., Zhang, Z., & Chen, X. (2025). Multi-elevation UAV-based frequency domain electromagnetic method for data calibration and field investigation. *Water Resources Research*, *61*, e2024WR039579. https://doi.org/10.1029/2024WR039579

Received 30 NOV 2024
Accepted 5 SEP 2025

Author Contributions:

Conceptualization: Qinbo Cheng, Andrew Binley, Xi Chen
Data curation: Zhicai Zhang
Formal analysis: Qinbo Cheng
Funding acquisition: Jintao Liu
Investigation: Qinbo Cheng, Zhijin Ma
Methodology: Qinbo Cheng
Project administration: Xi Chen
Resources: Qinbo Cheng
Software: Qinbo Cheng
Supervision: Andrew Binley
Validation: Qinbo Cheng, Andrew Binley
Visualization: Jiayun Chai
Writing – original draft: Qinbo Cheng

Abstract The Frequency Domain Electromagnetic Induction method (FDEM) is an efficient tool for investigating the electrical conductivity (EC) distribution over relatively shallow depths. However, the handheld method of use recommended by manufacturers does not fully leverage the non-invasive detection capabilities offered by FDEM devices. In this study, an unmanned aerial vehicle airborne FDEM (UAV-FDEM) system is introduced, which enables an operator to conduct investigations at specific flight heights along planned routes. Since multi-coil FDEM instruments typically experience consistency issues among different coils, we propose a calibration method based on a multi-elevation UAV-FDEM approach. The approach circumvents the need for geophysical inversion during calibration, and has been successfully employed to calibrate two multi-coil instruments. We tested the multi-elevation UAV-FDEM survey approach at two sites: a riparian zone of Yangtze River and a hot spring area in Tibet. The results show that the UAV-FDEM survey findings are comparable with those obtained using electrical resistivity tomography (ERT). The surveys detected temporal changes in soil EC that correspond with observed groundwater levels changes, and successfully delineated the intrusion area and subsurface path of geothermal water. In comparison to conventional ground-based single-elevation measurements, the multi-elevation UAV-FDEM method clearly improves the deterministic coefficients (that is measures of resolution) for the inverted EC value of different soil layers, and reduces the uncertainty of the geophysical inversion results. UAV-based FDEM surveys are efficient for large or inaccessible areas, but their application can be limited by adverse weather and restricted flight endurance.

Plain Language Summary Geophysical methods are now routinely used to measure the spatial (and temporal) variation of a proxy (e.g., electrical conductivity) that can often provide valuable insight into properties and states of interest (e.g., soil moisture, groundwater salinity, etc.). This study introduces an innovative method that uses drones equipped with an electromagnetic induction (EMI) instrument to map the electrical conductivity of shallow soils. Traditionally, EMI instruments are used as handheld devices and data are collected from one height above ground level. This can limit the amount of information obtained. In addition, in some cases access to areas of interest can be limited. In our new approach, drones fly along predetermined routes at different heights to collect multiple sets of EMI data. This multi-elevation strategy not only allows greater areal coverage but also improves the quality of the data by calibrating the measurements from the instrument's different sensors. Field tests were conducted at two locations-a riparian zone along the Yangtze River and a geothermal area in Tibet. The surveys reveal spatial variation in subsurface electrical conductivity that are related to the presence and movement of fluids in the ground. The drone-based EMI system offers a powerful tool for water resource management.

1. Introduction

Spatially continuity of subsurface properties and states are indispensable for addressing critical water resources challenges, including sustainable water supply planning, contaminant remediation, agricultural water management, watershed restoration, and streamflow forecasting. However, acquiring such data across large areas remains a persistent obstacle in hydrological practice. Soil electrical conductivity (EC), a proxy for soil moisture, pore water salinity, porosity, and clay content, offers a promising pathway to infer groundwater characteristics non-invasively (Binley et al., 2015; Binley & Slater, 2020; Robinson et al., 2008). While geophysical methods like

Writing – review & editing:
Qinbo Cheng, Andrew Binley, Xi Chen

electrical resistivity tomography (ERT) and vertical electrical sounding (VES) have been widely used to measure soil EC, electromagnetic induction (EMI) stands out as a rapid, non-contact, and scalable solution for generating high-resolution subsurface insights (Doolittle & Brevik, 2014; Robinson et al., 2008). By bridging the gap between geophysical innovation and hydrological applications, EMI-based approaches hold transformative potential for advancing groundwater monitoring and management—a cornerstone of modern water resources science and policy (Binley et al., 2015). Like many geophysical methods, recent developments in UAV-based approaches are offering greater potential for EMI application to water resource management. This paper develops advances to the implementation and analysis of UAV-based EMI measurements and illustrates these developments through two field-based investigations.

EMI is based on the induction principles defined by Faraday's law, and generally classified into two categories: Time-Domain and Frequency-Domain EMI that is, TDEM and FDEM (Boaga, 2017; Rubin & Hubbard, 2006). Because of self-transients caused by the self-inductance of transmitting loop, TDEM inevitably has a blind zone of exploration (Kamenetsky & Oelsner, 2000). Therefore, TDEM is typically used for relatively deep (several 10s m) investigations (Boaga, 2017), although recent instrument developments are beginning to address this limitation. In contrast, FDEM is widely employed for rapid surveying of the EC distribution of shallow soil layers, particularly in hydrological applications. In addition, airborne FDEM systems such as RESOLVE demonstrate the potential for deep investigations (Minsley et al., 2012). However, our focus is on multi-coil UAV-FDEM instruments, which avoid the frequency-dependent limitations of multi-frequency systems and are better suited for high-resolution, near-surface hydrological studies.

The basic principle of FDEM involves the transmitter coil (Tx) emitting an oscillating primary electromagnetic field (Hp) (Selepeng, 2016). This primary field induces eddy currents in the ground, with their strength depending on the medium's electrical conductivity. These eddy currents, in turn, emit a secondary magnetic field (Hs). Both the primary and secondary fields are measured at the receiver coil (Rx). From these measurements, the in-phase and quadrature (out-of-phase) components of the field ratio (Hs/Hp) are derived. The quadrature component is commonly used to estimate the apparent electrical conductivity (ECa), particularly under the low induction number (LIN) condition (McNeill, 1980). ECa represents a weighted average of EC values over a depth range, which varies with the Tx-Rx dipole center distance and the coil orientation for example, horizontal coplanar coil (HCP) and vertical coplanar coil (VCP) (Hanssens et al., 2019). It is important to note that we use ECa to represent the equivalent conductivity of a half-space starting directly beneath the instrument, which includes the air layer, as done by Andrade and Fischer (2018), for example.

The EM response measured by a FDEM system can be corrupted by various influences, such as base-level drift, primary-field removal, phase stability, close proximity of metallic objects, temperature and above-ground features (e.g., vegetation) (Blanchy et al., 2020; Lin et al., 2019; McLachlan et al., 2021). Therefore, it is usually necessary to calibrate the FDEM system. In particular, for multi-coil instruments, each coil may respond slightly differently, which has little impact when mapping relative contrasts but becomes critical when quantitative inversion is attempted. In such cases, careful calibration is essential to ensure consistency among coils and to obtain reliable subsurface conductivity estimates. Most FDEM manufacturers (e.g., GF Instruments, the manufacturer of the CMD-Explorer) recommend the use of a linear regression function with known subsurface EC values to correct ECa data (Lavoué et al., 2010; McLachlan et al., 2021; Tan et al., 2019). For this approach, the reliability of calibration results heavily depends on the measurement accuracy of the subsurface EC values. In order to enhance the calibration, some studies have incorporated other geophysical methods for example, ERT or VES (Blanchy et al., 2020; Lavoué et al., 2010; Von Hebel et al., 2019). However, these companion methods may introduce discrepancies due to differences in conduction pathways compared to FDEM (von Hebel et al., 2019). For instance, ERT relies on galvanic coupling, where current flow can be impeded by features like ground cracks, whereas FDEM employs inductive coupling, allowing eddy currents to form on both sides of such discontinuities, potentially leading to different EC readings. Therefore, ensuring the accuracy of the calibration approach using companion methods may be challenging.

Some manufacturers, such as DUALEM and Geonics, recommend positioning instruments at a sufficient height above ground level for calibration purposes (Abdu et al., 2007; Heil & Schmidhalter, 2019). For example, the "Roll Test of DUALEM Zero Settings" is based on the assumption that when the instrument is elevated high enough, measurements become uniform in all orientations. Similarly, the Geonics EM38-MK2 requires that the ECa reading in horizontal coplanar (HCP) mode be twice that in vertical coplanar (VCP) mode. This approach

relies on the principle that under LIN conditions and at an adequate elevation the cumulative sensitivity function in HCP mode is twice that in VCP mode. However, these calibration methods are practical only for instruments with shallow detection depths. For devices with larger detection ranges, such as GF Instruments' CMD-Explorer (which has a detection depth of 6.7 m), positioning the instrument 6.7 m above the ground is physically impractical, rendering these techniques unsuitable.

As the height of the instrument above the ground increases, the contribution of the high-sensitivity zone near the instrument decreases (since the EC of air is close to zero). Given the shape of the sensitivity function, this increase in elevation also increases the relative contribution of the deeper layer, leading to a larger depth of investigation of the instrument. Such multi-elevation measurement approaches have been widely used to correct ECa data collected by FDEM in recent years (Minsley et al., 2014; Tan et al., 2019). Several previous studies simultaneously inverted soil EC values using linear ECa correction model parameters in the geophysical inversion method (Minsley et al., 2014; Tan et al., 2019). However, with the introduction of additional parameters, such approaches may lead to enhanced uncertainty in the final model of EC variation.

At present, FDEM manufacturers do not offer equipment specifically designed for multi-elevation measurements. As a result, previous researchers have had to develop their own solutions, such as wooden racks with multiple steps (Tan et al., 2019). However, these non-standard devices are often too heavy or complex for field investigations over large areas. In addition, although some manufacturers provide harnesses to facilitate carrying FDEM for field surveys (Boaga, 2017; Doolittle & Brevik, 2014), there are significant drawbacks to the handheld FDEM method as recommended by manufacturers (De Smedt et al., 2016; Delefortrie et al., 2014, 2016). For example, it can be challenging to maintain the probe in a horizontal position and at a fixed height, and to investigate pre-planned routes (Saksa & Sorsa, 2017), which may be particularly important when conducting time-lapse surveys.

In contrast, airborne geophysical methods serve as effective tools to get regional survey information from the subwatershed to the basin scales (Robinson et al., 2008; Rubin & Hubbard, 2006; Siemon et al., 2009). In particular, there has been a recent surge in interest in the use of airborne EMI (FDEM and TDEM) for studies of groundwater hydrology. Piloted (helicopter and fixed wing aircraft) EMI surveys can provide unprecedented detail of the subsurface variation in EC over large scales, although such surveys have limited resolution of shallow (several meters) depth. Moreover, they are inevitably very expensive to conduct and typically not affordable for most studies.

Compared to piloted aircrafts, unmanned aerial vehicles (UAVs) are more convenient, mobile, safe and affordable, and have become valuable remote sensing platforms (Vélez-Nicolás et al., 2021). UAVs utilize automatic stabilization and control systems instead of manual operation, which can improve the physical stability (horizontality and rotation) of FDEM instruments. UAVs have been used as airborne platforms for FDEM devices, providing greater resolution of EC variation at shallow depths (compared to conventional airborne EMI). For example, Karaoulis et al. (2020) used a DJI Matrice 600 drone to mount the CMD-Mini-Explorer (GF Instruments) for distinguishing variations in EC due to freshwater—salinity contrasts as well as textural variation of field soils. Similarly, Mitsuhata et al. (2022) developed a drone-borne GEM-2 (Geophex, Ltd.) instrument to survey for buried metal objects and shallow soil EC distributions over relatively large areas. In a later study, Karaoulis et al. (2022) validated the performance of UAV-based CMD-Mini-Explorer and GEM-2 equipment through three field tests. More recently, Vilhelmsen et al. (2024) demonstrated the use of a drone-borne GEM-2 UAV sensor for subsurface characterization and archeological prospecting, highlighting its versatility in geophysical applications.

UAV deployed FDEM has a distinct advantage over the traditional ground-based approach, in that they do not require ground access to the survey area. This capability helps avoid disturbance and land degradation in sensitive or protected areas. There are, however, challenges with such an approach. One challenge is in-flight magnetic and electromagnetic interference signals (Walter et al., 2021). Most studies have shown that the electromagnetic interference decreases, as expected, with the separation distance between UAV and FDEM instrument (Karaoulis et al., 2020; Mitsuhata et al., 2022). There is an acceptable distance where the electromagnetic noise from the UAV appears to be negligible, for example, 0.75 m for R4 from Geosensors Inc., 6 m for GEM-2UAV from Geophex Ltd., 5 m for GEM-2, and 2 m for CMD-Mini-Explorer from GF Instruments (Bjerg et al., 2020; Karaoulis et al., 2020; Mitsuhata et al., 2022; Ralchenko et al., 2018). Generally, the acceptable distance between a UAV and FDEM instrument is approximately equal to the depth of investigation of the FDEM instrument.

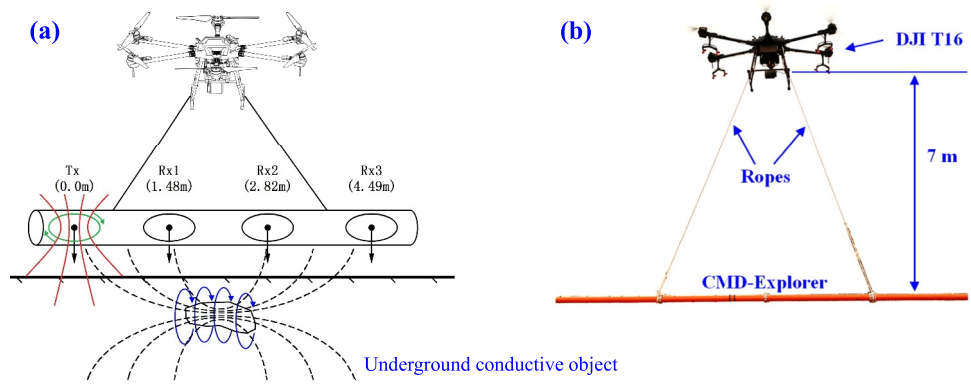

Figure 1. Principle and structure of a UAV-FDEM system: (a) sketch and (b) prototype setup. Green arrows in Tx coil indicate time varying current; red lines represent transmitted (or primary) EM radiations; blue lines depict induced electric currents; black dash lines show the induced (or secondary) magnetic field; black arrows indicate the perpendicular direction of coil faces, and numbers in brackets denote Tx-Rx coil separation distances.

Most previous UAV-FDEM studies have rarely considered the effect of flight height on survey results, and not clearly presented the advantages of UAV-based methods over the handheld approach in relation to the inversion results. In this study, we show a design for a UAV-FDEM system using a T16 drone (DJI Ltd.) to mount a CMD-Explorer (GF Instruments). We propose a new multi-elevation FDEM calibration method to detect and correct inconsistent ECa data and report on the effectiveness of this approach using ECa data collected by CMD-Mini-Explorer and CMD-Explorer devices. We also illustrate the multi-elevation UAV-FDEM method in a field study of a riparian zone of the Yangtze River in Nanjing and at a hot spring zone in Yangbajing, Tibet, and compare the inverted results with those from independent ERT surveys.

2. Methodology

2.1. Principle of Frequency Domain Electro-Magnetic Induction

For most FDEM devices (e.g., CMD-Explorer, DUALEM-2 and EM31 (Boaga, 2017; Doolittle & Brevik, 2014)), the transmitter (Tx) coil emits low frequency EM radiation, while the receiver (Rx) coil(s) detect superimposed EM radiation from two sources: Tx coil and underground electrical conductors, which generate EM radiation induced by the Tx coil, as shown in Figure 1a. Both primary and secondary field are recorded at the Rx coil and the quadrature and inphase component is computed.

For FDEM, there are two widely used forward models, that is, models that generate a measured ECa from a given distribution of soil EC. One is the one-dimensional Maxwell-based total solution for the magnetic field provided by Ward and Hohmann (1988). Because of the high accuracy and the wide applicable range, the Maxwell-based approach has been incorporated into FDEM inversion models, for example, the FEMIC code (Elwaseif et al., 2017) and EMagPy (McLachlan et al., 2021). However, this method poses certain challenges, mainly the higher computational demands arising from its non-linear nature. Therefore, a simpler method, known as the local-sensitivity model, was proposed by McNeill (McNeill, 1980). This method is based on the cumulative response of the subsurface layers and valid under the LIN condition (Selepeng, 2016). Its specific expression is as follows:

$$\boldsymbol{\sigma}_a = \int_{h_0}^{\infty} \phi(z/s)\boldsymbol{\sigma}\mathrm{d}z, \tag{1}$$

where $\boldsymbol{\sigma}_a$ is ECa (i.e., EC of homogeneous half-space that will give the same quadrature reading), $\boldsymbol{\sigma}$ is the EC of underground objectives, $\phi(z/s)$ is the local-sensitivity function evaluated at z/s (of which z and s are the depth below the FDEM probe and the Tx-Rx coil separation, respectively), and h_0 is the height of FDEM probe above the ground surface.

2.2. Multi-Elevation FDEM Measurements Using an Unmanned Aerial Vehicle

Most modern FDEM instruments provide simultaneous measurements using more than one Tx-Rx coil separation, or coil orientation. Increasing the separation between the Tx and Rx coils extends the depth of investigation by probing a larger volume (geometrical sounding). The orientation of the Tx and Rx coils also affects the depth of investigation. In the horizontal coplanar (HCP) mode both Tx and Rx coils have horizontal windings. In the vertical coplanar (VCP) model, the windings are vertical, which results in a shallower depth of investigation compared to HCP for the same Tx-Rx coil separation. The GF Instruments CMD-Explorer and CMD-Mini-Explorer can be used in HCP or VCP mode. In contrast, the DUALEM-2 measures simultaneously in both HCP and perpendicular geometry (PRP), with the latter using Tx in horizontal orientation and Rx in vertical orientation. In addition to coil separation and orientation, the operating frequency can also be varied to control the depth of investigation, as implemented in systems such as GEM-2 or RESOLVE.

The measurement of more than one Tx-Rx coil separation, or coil orientation allows, in theory, the application of an inverse method to determine some information about vertical variation in soil EC at the measurement location. For the three Rx coil CMD-Explorer and CMD-Mini-Explorer (GF Instruments), three measurements are obtained. These measurements can then be used to determine the EC for a two-layer EC model, along with the thickness of the upper layer. However, such a result is likely to be subject to high uncertainty. In order to increase the amount of data for FDEM inversion, the multi-elevation method is an effective approach to reveal the soil layer information at different depths, as the local sensitivity functions with respect to soil depth are nonlinear (McNeill, 1980). However, conducting multi-elevation measurements in the field manually is challenging, particularly for investigations to depths of several meters. Therefore, we have developed a solution that uses a UAV-mounted FDEM probe (Figure 1), which we call the multi-elevation UAV-FDEM.

In this UAV-FDEM system, an 8.0 kg CMD-Explorer (GF Instruments) was suspended from a DJI T16 UAV by two ropes, each 7 m in length, to avoid electromagnetic interference from the UAV, as shown in Figure 1b. The "GPS Continuous Measurement" mode of the CMD-Explorer, utilizing time-triggered measurements at 0.3-s intervals, was employed in this study. The DJI T16 UAV used was chosen because of its high-accuracy positioning system, which includes the real-time kinematic positioning technique (RTK) and a radar altimeter, and provides both horizontal and vertical positional accuracies of ±0.1 m. Additionally, the UAV has a maximum load capacity of 16 kg and a hovering time of about 10–18 min. Due to the payload impact of FDEM, the actual flight endurance of the UAV-FDEM system in this study is approximately 10 min per detection mission. The remote controller of the UAV allows the operator to plan the flight route and survey height. Considering the temperature sensitivity of the FDEM instrument, this study recommends allowing the device to warm up before use by powering it on and allowing sufficient time for the sensor temperature to stabilize at ambient conditions.

Due to incompatible data protocols between the UAV and FDEM system, establishing direct communication was challenging. To address this, an RTK system (S86; South Surveying & Mapping, China) with horizontal and vertical positional accuracies of ±0.01 and ±0.03 m, respectively, was mounted atop the UAV. This system provided the FDEM measurements with real-time positional information via Bluetooth. To account for measurement errors in instrument height and mitigate their influence, we used the mean of all ECa observations within a specified height interval. For instance, ECa data at a nominal height of 1 m were represented by the average of observations collected within the (0.75, 1.25 m) range.

The FDEM control unit is directly installed on the probe, as the CMD-Explorer provides a designated mounting position. And the "F-ground" setting is chosen for the ECa data collection. The UAV-based FDEM deployment provides clear benefits, such as reduced human-related errors, minimal land impact, higher operational efficiency, and expanded survey coverage. A potential limitation is the need for additional instrumentation and, in some cases, regulatory approval. Users should consider these trade-offs when planning UAV-FDEM surveys.

For the UAV-FDEM system in this study, there are two measurement modes: point and route. In the point measurement mode, the UAV slowly raises the FDEM vertically from a stationary position, allowing FDEM measurements at different instrument heights (in our case from 0 to 7 m). Because the point mode can continuously collect the ECa values at various heights, it is suitable for detailed investigations or FDEM calibration. In the route measurement mode, the UAV carries the FDEM along the planned flight path at pre-defined heights. The route measurement method, therefore, permits mapping at the field scale. Due to the large spatial footprint of the FDEM system, motion-induced artifacts in FDEM readings were not explicitly addressed in this study (Huang

et al., 2014). As the UAV-mounted instrument can exhibit oscillation during take-off, landing, and turning, we recommend excluding data collected during these unstable flight phases to ensure that only stable and reliable measurements are retained for analysis.

Based on the multi-elevation UAV-FDEM system, we can collect ECa data in multi-configuration scenarios (i.e., multi-height, -coil and –mode such as HCP and VCP). For these data, we can build a simple model according to the local-sensitivity model (Equation 1) in the layered soil. Its discrete formula is as follows:

$$\begin{bmatrix} R\left(\frac{h_1}{s_1}\right)-R\left(\frac{h_1+z_1}{s_1}\right) & \cdots & R\left(\frac{h_1+z_{n-2}}{s_1}\right)-R\left(\frac{h_1+z_{n-1}}{s_1}\right) & R\left(\frac{h_1+z_{n-1}}{s_1}\right) \\ \vdots & \ddots & \vdots & \vdots \\ R\left(\frac{h_m}{s_1}\right)-R\left(\frac{h_m+z_1}{s_1}\right) & \cdots & R\left(\frac{h_m+z_{n-2}}{s_1}\right)-R\left(\frac{h_m+z_{n-1}}{s_1}\right) & R\left(\frac{h_m+z_{n-1}}{s_1}\right) \\ R\left(\frac{h_1}{s_2}\right)-R\left(\frac{h_1+z_1}{s_2}\right) & \cdots & R\left(\frac{h_1+z_{n-2}}{s_2}\right)-R\left(\frac{h_1+z_{n-1}}{s_2}\right) & R\left(\frac{h_1+z_{n-1}}{s_2}\right) \\ \vdots & \ddots & \vdots & \vdots \\ R\left(\frac{h_m}{s_p}\right)-R\left(\frac{h_m+z_1}{s_p}\right) & \cdots & R\left(\frac{h_m+z_{n-2}}{s_p}\right)-R\left(\frac{h_m+z_{n-1}}{s_p}\right) & R\left(\frac{h_m+z_{n-1}}{s_p}\right) \end{bmatrix} \begin{bmatrix} \sigma_1 \\ \vdots \\ \sigma_i \\ \vdots \\ \sigma_n \end{bmatrix} = \begin{bmatrix} \sigma_{a,1} \\ \sigma_{a,m} \\ \sigma_{a,m+1} \\ \sigma_{a,m\times p} \end{bmatrix}, \quad (2)$$

where m, p and n are the number of FDEM probe height, Rx coils and soil layers, respectively, h_i, s_i, z_i, σ_i, and $\sigma_{a,i}$ are the ith FDEM probe height, Tx-Rx coil separation, underground depth, EC and ECa, respectively, and $R(x)$ is the cumulative sensitivity function evaluated at x:

$$R(x) = \int_x^{\infty} \phi(z)\, dz, \quad (3)$$

Equation 2 can be abbreviated as:

$$\boldsymbol{A}\,\boldsymbol{\sigma} = \boldsymbol{\sigma}_a, \quad (4)$$

where $\boldsymbol{A}$ is a $mp \times n$ sensitivity matrix, $\boldsymbol{\sigma}$ is the EC vector of soil layers, and $\boldsymbol{\sigma_a}$ is the ECa vector collected by the FDEM device.

2.3. FDEM Measurement Correction by Multi-Elevation Approach

For the multi-coil FDEM system (Figure 1a), the Rx coils operate independently of one another, however, this independence may introduce systematic errors into the measurements, and these different errors per coil matters more when you want to bring their information together in an inversion. In a number of previous studies, linear regression has been used to calibrate each Rx coil in turn (McNeill, 1980; McLachlan et al., 2021):

$$\boldsymbol{\sigma}_a = a \times \boldsymbol{Q} + b, \quad (5)$$

where a and b are parameters, and $\boldsymbol{Q}$ is the output data of a Rx coil, which may vary between instruments and can represent either the out-of-phase value or ECa.

The parameters (i.e., a and b) in Equation 5 can be estimated by the least squares approach using FDEM measurements taken from various testing samples that have known EC values (McLachlan et al., 2021). This method calibrates each Rx coil independently, which may lead to inconsistent FDEM measurements among different Rx coils because of various influence factors in practice such as base-level drift, electromagnetic interference and small differences in Tx–Rx coil separation.

Given the potential for inconsistent behavior, a new calibration approach with multi-elevation measurements is proposed in this study, which employs the Singular Value Decomposition (SVD) technique (Stewart, 1993) to analyze all ECa data (Equation 4), thereby addressing the inconsistency issues present in FDEM calibrations. The

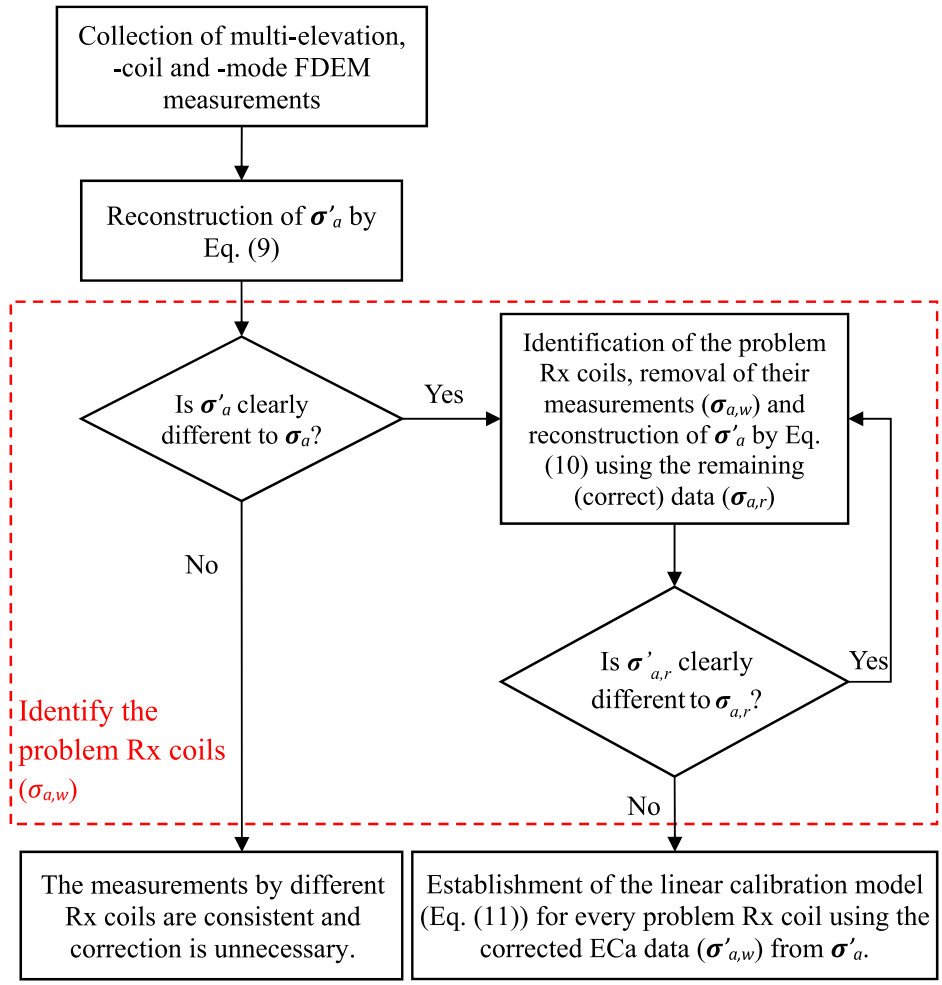

Figure 2. Flow chart of the new calibration method for multi-coil FDEM.

SVD method was selected in this study due to the alignment of its core assumptions (e.g., system linearity, noise independence) with the theoretical framework of the FDEM system described in Equation 4. The detailed procedures of the new calibration method are illustrated in Figure 2. In this figure, the multi-elevation calibration approach first finds out the inconsistent ECa data by comparison of the reconstructed ($\boldsymbol{\sigma}'_a$) with the measured ECa ($\boldsymbol{\sigma}_a$), and then according to this comparison, identifies the problematic Rx coils, next removes the $\boldsymbol{\sigma}_{a,w}$ measured by the problematic Rx coils. The method then uses the remaining valid ECa data ($\boldsymbol{\sigma}_{a,r}$) to predict the correct values ($\boldsymbol{\sigma}'_{a,w}$) for $\boldsymbol{\sigma}_{a,w}$, and finally separately establishes the linear calibration model for each problematic Rx coil using the corrected ECa data ($\boldsymbol{\sigma}'_{a,w}$) derived from $\boldsymbol{\sigma}'_a$. The core concept of the SVD-based method is that the multi-configuration setup of the FDEM instrument (involving different heights, coil orientations, and coil offsets) inherently generates a degree of informational redundancy. This redundancy is then exploited to evaluate the consistency of measurements across different coil offsets. Importantly, the redundancy is determined by the rank of the sensitivity matrix A (Equation 4) rather than by the magnitude of the ECa values recorded by the FDEM instrument. The mathematical foundation of the new method is detailed below.

The expression of SVD for the sensitivity matrix $\boldsymbol{A}$ in Equation 4 is as follows:

$$\boldsymbol{A} = \boldsymbol{U} \times \boldsymbol{\Sigma} \times \boldsymbol{V}^T, \tag{6}$$

where $\boldsymbol{U}$ is a $mp \times mp$ orthogonal matrix, $\boldsymbol{\Sigma}$ is a $mp \times n$ rectangular diagonal matrix with non-negative real numbers on the diagonal, $\boldsymbol{V}$ is a $n \times n$ orthogonal matrix.

As shown in Equation 6, the diagonal entries in $\boldsymbol{\Sigma}$ are known as the singular values of sensitivity matrix $\boldsymbol{A}$ in Equation 4. The number of non-zero singular values in $\boldsymbol{\Sigma}$ is equal to the rank of $\boldsymbol{A}$. The columns of $\boldsymbol{U}$ and $\boldsymbol{V}$ are called as the left-singular vectors and the right-singular vectors of $\boldsymbol{A}$, respectively. $\boldsymbol{A}$ can be approximately reconstructed by omitting some small singular values in $\boldsymbol{\Sigma}$ (Equation 6):

$$\boldsymbol{A} \approx \hat{\boldsymbol{U}} \times \hat{\boldsymbol{\Sigma}} \times \hat{\boldsymbol{V}}^T, \tag{7}$$

where $\hat{\boldsymbol{U}}$ is a $mp \times r$ orthogonal matrix extracted from $\boldsymbol{U}$, $\hat{\boldsymbol{\Sigma}}$ is a $r \times r$ rectangular diagonal matrix from $\boldsymbol{\Sigma}$, $\hat{\boldsymbol{V}}$ is a $n \times r$ orthogonal matrix from $\boldsymbol{V}$. Here, r represents the number of selected singular values that is, the rank of approximation matrix of $\boldsymbol{A}$.

We substitute Equation 7 into Equation 4, which yields:

$$\hat{\boldsymbol{U}} \times \hat{\boldsymbol{\Sigma}} \times \hat{\boldsymbol{V}}^T \times \boldsymbol{\sigma} \approx \boldsymbol{\sigma}_a \,. \tag{8}$$

According to Equation 8, ECa (i.e., $\boldsymbol{\sigma}_a$) measured by FDEM can be reconstructed by the least squares method (of which the complete derivation is provided in the Text S1 of Supporting Information S1 for further reference):

$$\boldsymbol{\sigma}'_a = \left(\hat{\boldsymbol{U}} \times \hat{\boldsymbol{\Sigma}}\right)\left[\left(\hat{\boldsymbol{U}} \times \hat{\boldsymbol{\Sigma}}\right)^T\left(\hat{\boldsymbol{U}} \times \hat{\boldsymbol{\Sigma}}\right)\right]^{-1}\left(\hat{\boldsymbol{U}} \times \hat{\boldsymbol{\Sigma}}\right)^T \boldsymbol{\sigma}_a, \tag{9}$$

where $\boldsymbol{\sigma}'_a$ is a vector that is calculated by Equation 9 using the measurement ECa ($\boldsymbol{\sigma}_a$) values, which can be termed the reconstructed ECa.

According to Equation 9, if the measured ECa ($\boldsymbol{\sigma}_a$) values from different Rx coils are consistent, the reconstructed ECa ($\boldsymbol{\sigma}'_a$) should be equal or close to the corresponding $\boldsymbol{\sigma}_a$. Otherwise, if discrepancies are observed, this suggests the presence of inconsistent measurements. In such cases, we identify the problematic Rx coils according to the inconsistent measurements, and remove the corresponding ECa data ($\boldsymbol{\sigma}_{a,w}$) collected by those coils. Subsequently, we reconstruct ECa data ($\boldsymbol{\sigma}'_a$) using the remaining valid ECa data ($\boldsymbol{\sigma}_{a,r}$) (of which the complete derivation is provided in the Text S2 of Supporting Information S1 for further details):

$$\boldsymbol{\sigma}'_a = \left(\hat{\boldsymbol{U}} \times \hat{\boldsymbol{\Sigma}}\right)\left[\boldsymbol{M}^T\boldsymbol{M}\right]^{-1}\boldsymbol{M}^T\boldsymbol{\sigma}_{a,r}, \tag{10}$$

where $\boldsymbol{\sigma}'_a$ is the reconstructed ECa using $\boldsymbol{\sigma}_{a,r}$, which consists of the reconstructed correct-ECa ($\boldsymbol{\sigma}'_{a,r}$) and the reconstructed inconsistent-ECa ($\boldsymbol{\sigma}'_{a,w}$), $\boldsymbol{M}$ is a $q \times r$ matrix extracted from the matrix $\hat{\boldsymbol{U}} \times \hat{\boldsymbol{\Sigma}}$ according to the row sequence number of $\boldsymbol{\sigma}_{a,r}$ in $\boldsymbol{\sigma}_a$, and q is the vector length of $\boldsymbol{\sigma}_{a,r}$.

If $\boldsymbol{\sigma}'_{a,r}$ is equal or close to the $\boldsymbol{\sigma}_{a,r}$, we can treat the $\boldsymbol{\sigma}'_{a,w}$ as the correct or consistent values. And then a linear calibration model for the problematic Rx coils can be built using the corrected ECa values ($\boldsymbol{\sigma}'_{a,w}$):

$$\boldsymbol{\sigma}'_{a,w,i} = a_i \times \boldsymbol{\sigma}_{a,w,i} + b_i, \tag{11}$$

where $\boldsymbol{\sigma}'_{a,w,i}$ and $\boldsymbol{\sigma}_{a,w,i}$ are the vectors of corrected and original ECa data measured by the ith Rx coil, respectively, a_i and b_i are parameters of the linear calibration model for the ith Rx coil.

For the SVD method, the rank (i.e., r in Equation 6) of the approximation of matrix $\boldsymbol{A}$ (Equation 7) should be determined first. This value can be estimated using a modeling test. In this test we constructed an ideal semi-infinite stratum model, where there are 100 soil layers, each with 0.07 m thickness and uniform EC value. The forward model (Equation 2) was employed to simulate the ECa data collected by a CMD-Explorer within a probe height range of 0–7 m at elevation steps of 0.05 m. The synthetic ECa data ($\boldsymbol{\sigma}_a$) with different coil separations, coil orientations and probe heights were then utilized to reconstitute $\boldsymbol{\sigma}_a$ (denoted as $\boldsymbol{\sigma}'_a$, Equation 9). The mean relative error (e) of $\boldsymbol{\sigma}'_a$ was calculated to evaluate the effect of matrix rank (r, representing the number of singular values in Equation 6):

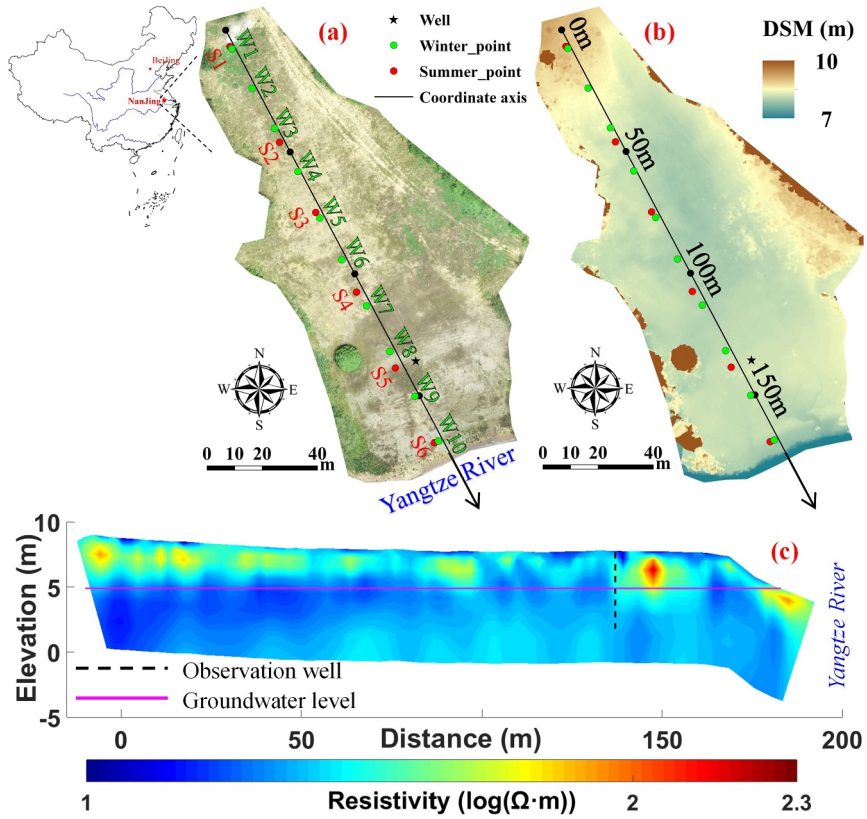

Figure 3. Location and geographical features of the riparian transect: (a) orthophoto; (b) digital surface model generated by DJI Terra software using aerial photos collected by DJI Phantom UAV; (c) investigation result of ERT along the survey line in winter. Red and green symbols represent the measurement points in summer and winter, respectively. These points are numbered sequentially from the riparian zone to the Yangtze River. The black symbols indicate the scaling points of the survey line. The dash line represents the observation well, and the magenta line indicates the inferred groundwater level based on the well observation.

$$e = \overline{\left|\frac{\boldsymbol{\sigma}_a' - \boldsymbol{\sigma}_a}{\boldsymbol{\sigma}_a}\right|}. \tag{12}$$

Our calculations revealed a significant inverse relationship between e and r, where e diminishes with increasing r. However, it is well known that the uncertainty associated with the least squares method, as described in Equations 9 and 10 for ECa reconstruction, increases with the number of singular values (i.e., the number of unknown parameters). When r is greater than or equal to 5, e is less than 0.1%, which is generally small enough for the most cases of approximate evaluation. Therefore, five singular values in $\boldsymbol{\Sigma}$ (i.e., $r = 5$ in Equation 6) are utilized in this study for the approximate estimation of $\boldsymbol{A}$ (Equation 4) and the reconstruction of ECa (Equations 9 and 10).

3. Test Area

We tested the UAV-FDEM method at two field sites: one located at a riparian transect adjacent to the Yangtze River in Nanjing, China, and the other at the Yangbajing thermal spring area in Tibet, China.

3.1. Field Site 1: Riparian Transect

Field site 1 is situated at the riparian zone of Yangtze River downstream in Nanjing, China (Figures 3, 118°50′5.3″E, 32°10′5.0″N). The area is part of the flood plain of Yangtze River, where the primary soil type is loamy sand. On 4 June 2021 (summer), we used a DJI Phantom UAV to capture aerial photos of this area, and then employed the DJI Terra software to generate an orthophoto (Figure 3a) and a digital surface model (DSM, Figure 3b). The aerial survey results show that the test area is relatively flat, covered with some weeds (e.g.,

Wormwood and Setaria), and surrounded by trees (e.g., Willow and Camphor). An observation well is located near the UAV-FDEM survey line (black asterisk in Figure 3).

The groundwater table depths (from ground level) in the observation well were measured at 1.34 m in the summer (i.e., 4 June 2021) and 3.15 m in the winter (i.e., 28 December 2021). The EC of groundwater (measured by an EC300A m, EcoSense Instruments) was 90 mS/m in summer and 99 mS/m in winter, indicating moderately electrically conductive groundwater. The measurements indicate that both the groundwater depth and the EC value in winter are greater than those in summer. As the test area is adjacent to the Yangtze River, the groundwater table in the study area may be roughly horizontal, and thus the well observation results can be used to estimate the local groundwater level (magenta line in Figure 3c). ERT measurements were conducted using a Syscal Pro switch 96 (IRIS Instruments) to investigate the subsurface features along the survey line (Figure 3a) in winter. The ERT survey used 96 electrodes, spaced 2 m apart, employing measurement modes in a dipole-dipole configuration with current and voltage dipole width of 2, 4 and 6 m. The ERT image (Figure 3c) reveals a distinct boundary between the resistive and conductive areas, which possibly represents the boundary between the unsaturated and saturated zones, consistent with the inferred groundwater level (magenta line in Figure 3c) based on the single well observation. Note that the relatively coarse texture of the local soils is likely to lead to a distinctive contrast in electrical conductivity at the water table. Such contrast is unlikely to exist in more fine textured soils because of thicker capillary fringe.

The UAV-FDEM was used to investigate the study area in both summer and winter, as shown in Figure 3a. We chose several test points (i.e., six red symbols in summer and 10 green symbols in winter) that were evenly distributed along the survey line, and conducted measurements at these points using the point measurement mode of UAV-FDEM. Next, we employed the route measurement mode to scan the study area along the survey line at different given flight heights in summer. For the VCP mode, the heights ranged from 0.6 to 2.7 m, with an interval of 0.1 m (a total of 22 heights), while for the HCP mode, the heights ranged from 0.6 to 4.9 m, also with an interval of 0.1 m (a total of 44 heights). The flight velocity was set to 1.0 m/s, with a time interval of 0.3 s between FDEM records.

3.2. Field Site 2: Hot Spring Area

The studied hot spring area is located at the southern foot of Nyenchen-Tanglha Range, and close to the Yangbajing geothermal power plant at Dangxiong County in Tibet, China (Figure 4, 90°28′46.0″E, 30°3′55.0″N). The study area is part of the proluvial-alluvial plain, where the predominant soil type is loamy sand. Previous studies reveal that the hot spring mainly derives from deep-circulating local groundwater, where water (such as glacier melt, snowmelt and rainfall) from the mountain areas infiltrates into the deep magma zone along fractures and then gets heated, flows downwards, and finally discharges in springs in the valley along the fractures or conduits (Guo et al., 2007).

On 28 July 2021, we employed a UAV (DJI Phantom 4 RTK) to capture aerial photos in this area. These photos were subsequently processed using DJI Terra software to generate an orthophoto (Figure 4a) and a Digital Surface Model (DSM, Figure 4b). Figure 4a shows that the study area is predominantly barren land, with a mean NDVI (Normalized Difference Vegetation Index) value of only 0.17, possibly because of the deep groundwater levels and the saline-alkali soils influenced by hot springs. The predominant vegetation in this area consists mainly of weeds such as Elymus sibiricus. The DSM (Figure 4b) illustrates that the ground altitude gradually decreases from northwest to southeast, with two streams running northwest to southeast across the region.

There is an artesian well (i.e., the blue symbol in Figure 4a and photo in Figure 4c) located at the northeast corner, along with several rising springs (red symbol in Figure 4a and photo in Figure 4d) in the low-lying area. The altitude of artesian well is significantly higher than that of the hot springs. Specifically, the altitude of artesian well is about 4,252.3 m, while the altitudes of the hot springs are below 4,250.3 m. The mean EC and temperature values of water in hot springs are 280 mS/m and 77°C, respectively, both of which are lower than those in the artesian well, where they are 440 mS/m and 87°C, respectively. This difference might be due to the artesian well's water mixing with less fresh groundwater compared to the hot springs.

ERT was used to investigate the subsurface features along the survey line (i.e., red line in Figure 4). The ERT survey utilized 96 electrodes spaced 5 m apart, employing measurement modes in a dipole-dipole configuration with current and voltage dipoles 5, 10 and 15 m in width. The results from the ERT survey are presented in

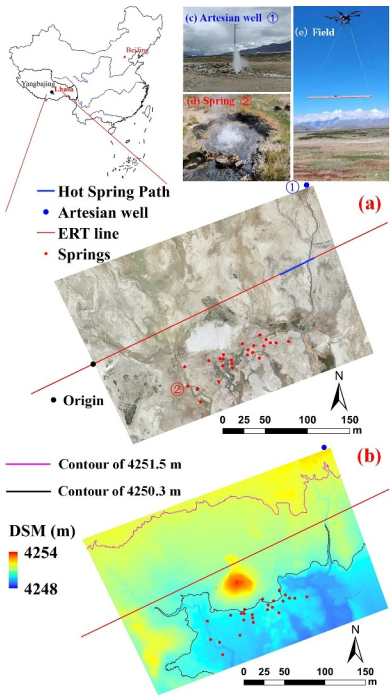

Figure 4. Location and geographic features of hot spring area at Yangbajing, in Tibet, China: (a) aerial orthophoto; (b) digital surface model (DSM); (c) a scene photo of artesian well; (d) a photo of hot spring; (e) a field test photo of UAV-FDEM. The blue symbol represents the artesian well, red symbols indicate the hot springs, and the black symbol marks the origin of the ERT survey line. The red line represents the ERT survey line, and the blue line depicts the inferred hot water upwelling path based on ERT investigation results (Figure 5). The magenta and black lines are the DSM contour lines at 4,251.5 and 4,250.3 m above sea level, respectively.

Figure 5, which reveals a high EC zone (i.e., the red circle where the EC value is more than 160 mS/m) located approximately 15 m below the ground surface. This zone might represent a hot water conduit connected with the artesian well (i.e., the blue symbol in Figure 4). The area with high EC enclosed by the EC contour line of 100 mS/m (i.e., the magenta line) signify the zone where hot water invades the subsurface. Figure 5 suggests that the spread of hot water might be restricted by a low-permeability soil layer characterized by high resistivity. A fractured section of this inferred low permeability layer, located about 5 m below ground surface, likely serves as the pathway for hot water upwelling. According to the ERT survey results, the formation of hot springs in the lowland areas might be attributed to the absence or disruption of a shallow low-permeability layer.

In order to understand the subsurface path of hot water and identify the spring area, the multi-elevation UAV-FDEM was employed to investigate the study area (Figure 4e). We programmed 22 parallel flight routes spaced 10 m apart and aligned with the upper boundary of the study area. The multi-elevation UAV-FDEM method with the route measurement mode was used to scan the study area along the survey line at different given flight heights that is, 0.4, 0.6, 0.9, 1.1, 1.6, 2.1, 2.6 and 3.1 m (a total of 8 heights) for HCP mode, and 0.6, 0.8, 1.1, 1.6, 2.1 and 2.6 m (a total of 6 heights) for VCP mode. The flight velocity was set to 4.0 m/s, with a time interval of 0.3 s for FDEM records.

4. Results

4.1. Correction of FDEM Using the Multi-Elevation Measurement Method

4.1.1. Calibration of CMD-Mini-Explorer Instrument

Tan et al. (2019) presented a set of FDEM data collected by CMD-Mini-Explorer with different configurations (e.g., six Rx coils, HCP and VCP modes and six probe heights) at five measurement points (i.e., CP1 - CP5 in Figure 6). At each point, they collected 72 ECa measurements. They utilized a combined inversion method for the layered soil EC values and the linear correction model parameters to calibrate the CMD-Mini-Explorer. However, this approach may yield high uncertainty because of the ill-posedness and non-uniqueness problems associated with the inverse method used. In this study, we first extracted the FDEM data collected by Tan et al. (2019) and used these data to reconstruct the ECa values by Equation 9 as shown in Figure 6. This figure indicates that some data points from the coil separations of 1.8 and 1.35 m in the HCP mode (i.e., HCP_s1.80 and HCP_s1.35)

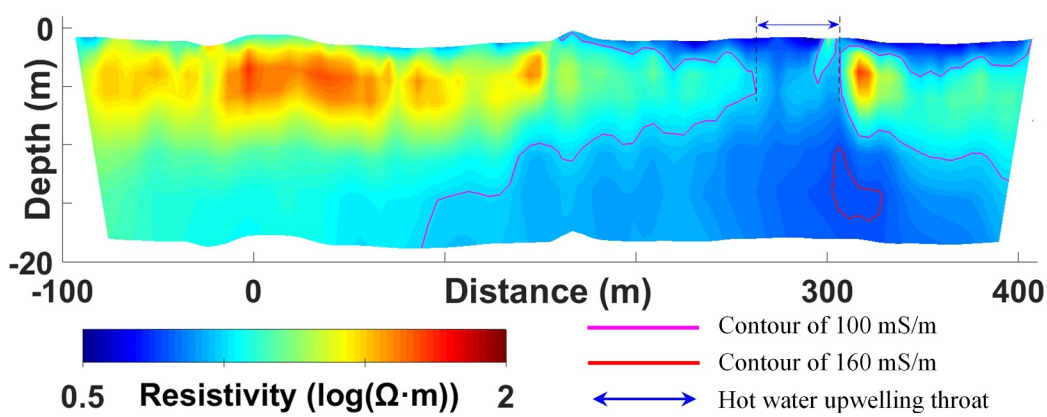

Figure 5. Investigation results of ERT along the survey line in the hot spring area (Figure 4). The magenta and red lines represent the EC contour lines of 100 and 160 mS/m, respectively. The double arrowhead line between two dash lines indicates a possible hot water upwelling pathway.

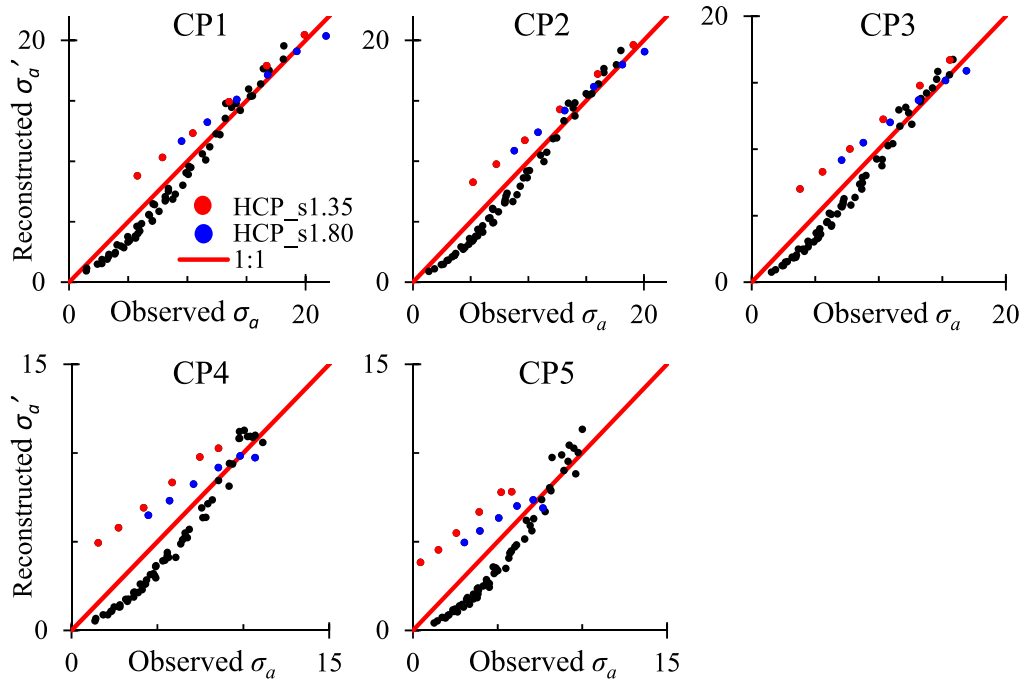

Figure 6. Comparison of the reconstructed and the observed ECa data (mS/m) for CMD-Mini-Explorer at five sites from Tan et al. (2019). The red and blue symbols represent the ECa data collected by HCP_s1.35 and HCP_s1.80, respectively, while the black symbols indicate the ECa data from other configurations. The red line is the 1:1 line.

obviously deviate from the 1:1 line. In other words, the HCP_s1.80 and HCP_s1.35 ECa data may be inconsistent with the other data (i.e., those from other configurations).

After removing the ECa data measured by HCP_s1.80 and HCP_s1.35, we reconstructed the ECa data by Equation 10 using the remaining data, and then compared the reconstructed data ($\sigma'_{a,r}$) with the observed data ($\sigma_{a,r}$) as shown in Figure 7. In this figure, most points cluster around the 1:1 line (Figure 7), indicating consistency between the reconstructed ECa data and the FDEM theoretical model (Equation 2). The Root Mean Square Error (RSME) between the reconstructed and observed ECa improved from 1.4 mS/m (Figure 6) to 0.8 mS/m (Figure 7), highlighting the efficacy of the inconsistent data removal. Therefore, the ECa data for HCP_s1.80 and HCP_s1.35, predicted by Equation 10 using the remaining data (excluding those from HCP_s1.80 and HCP_s1.35), can serve as calibration targets for the inconsistent data.

The predicted ($\sigma'_{a,w}$ by Equation 10) versus the measured ECa ($\sigma_{a,w}$) data for HCP_s1.80 and HCP_s1.35 from all five sites are presented in Figure 8. This figure clearly shows a linear relationship between the predicted (i.e., correct) and the original ECa data. Thus, the linear regression model (Equation 11) can be used to calibrate the measurements of HCP_s1.80 and HCP_s1.35 as shown in Figure 8, which is in agreement with previous studies (Tan et al., 2019).

4.1.2. Calibration of CMD-Explorer Instrument

The investigation results of UAV-FDEM with point measurement mode at six sites (i.e., red symbols in Figure 3) in summer were used to validate the CMD-Explorer measurements. In this UAV airborne system (Figure 1), the CMD-Explorer (equipped with three Rx coils and two coil orientations i.e., HCP and VCP modes) collects ECa data at flight heights ranging from 0 to 7 m with an interval of 0.05 m. At each measurement point, a total of 846 ECa data points can, therefore, be collected. These data are then used to reconstruct ECa values by Equation 9. The relationship between the reconstructed (σ'_a) and the observed ECa (σ_a) data at six sites is shown in Figure 9. In this figure, the points from the Rx coil with a dipole center distance of 4.49 m under the HCP mode (i.e., HCP_s4.49) obviously deviates from the 1:1 line, which means that the ECa data of HCP_s4.49 are inconsistent with other ECa data and need to be corrected.

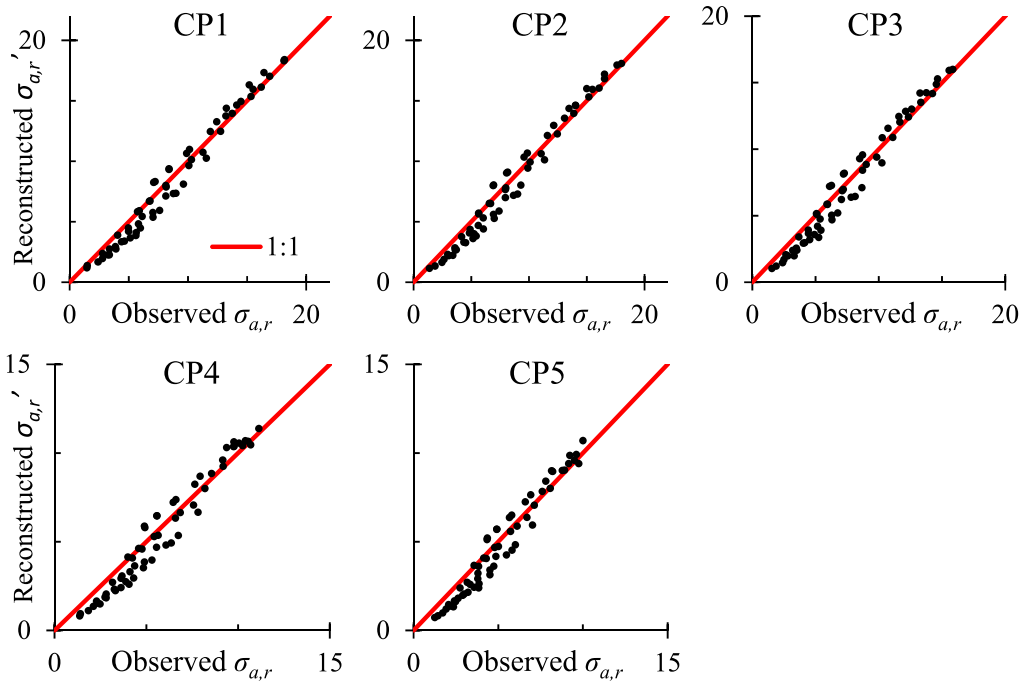

Figure 7. Comparison of the reconstructed and the observed ECa data (mS/m) after elimination of the inconsistent data from HCP_s1.35 and HCP_s1.80. The red line represents the 1:1 line.

After removing the ECa data from HCP_s4.49, the remaining data were used to reconstruct the ECa data by Equation 10. The RSME between the reconstructed and observed ECa improved from 1.0 mS/m (Figure 9) to 0.56 mS/m, suggesting that the rest of the ECa data are consistent and meet the FDEM theoretical model (Equation 2). Therefore, the reconstructed ECa data can be considered to be correct, and then the ECa data of HCP_s4.49 predicted by Equation 10 can be treated as the calibration objectives.

The predicted ECa data of HCP_s4.49 by Equation 10 at all six sites (Figure 3) were compared with the observed data as shown in Figure 10a. In this figure, for large ECa values collected at the low probe heights, there are clearly non-unique and non-linear relationships between the predicted and the observed data for HCP_s4.49. This discrepancy may arise from several factors affecting FDEM measurements at low probe heights, including: (a) imperfect cancellation of the primary magnetic field (i.e., the free-space field generated by the transmitter coil), which can dominate the secondary field signal; (b) variability in the quadrature response stability due to electronic drift or environmental noise; (c) instrument tilting or rolling, which alters the effective coil-soil geometry, particularly when closer to the surface; and (d) interference from above-ground features (e.g., vegetation). After removing the ECa data collected at probe heights lower than 0.5 m, a clear linear relationship emerges between

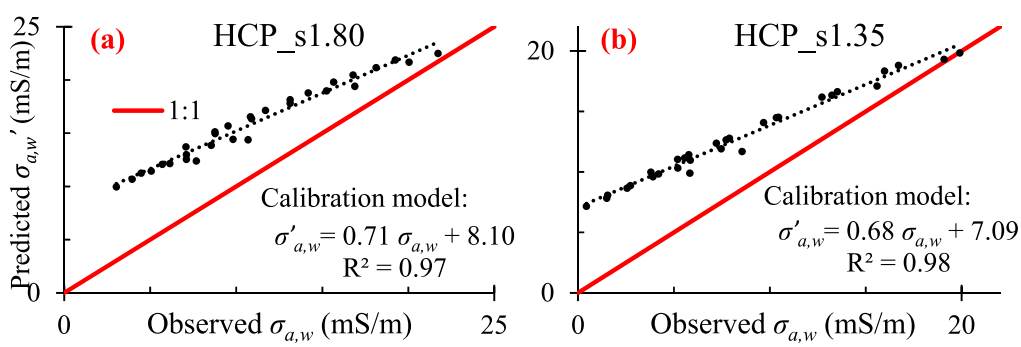

Figure 8. Calibration of the ECa data collected by HCP_s1.80 and HCP_s1.35 using the predicted ECa values by Equation 10: (a) HCP_s1.80; (b) HCP_s1.35. The red line represents the 1:1 line.

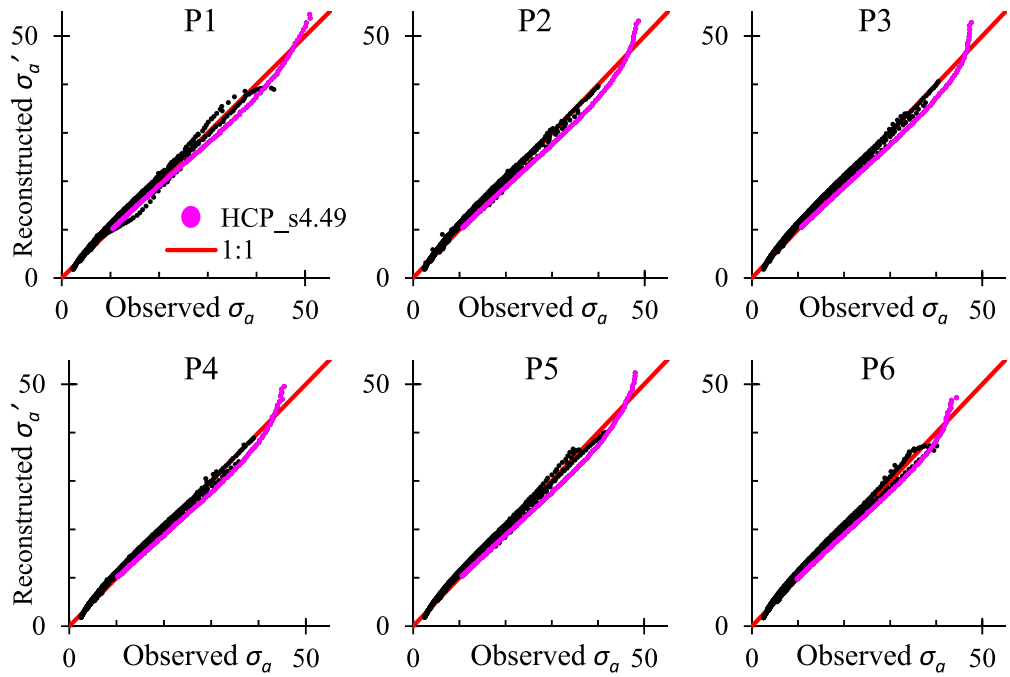

Figure 9. Comparison of the reconstructed and the observed ECa data (mS/m) from the CMD-Explorer at six sites (Figure 3) in summer. The magenta symbols represent the ECa data from HCP_s4.49, while the black symbols represent the remaining ECa data from the other coil configurations. The red line indicates the 1:1 line.

the predicted and observed data, as shown in Figure 10b. Therefore, the linear regression model (Equation 11) can be used to correct the ECa data measured by HCP_s4.49 at the high probe heights, while the ECa data collected by HCP_s4.49 at the low probe heights (e.g., lower than 0.5 m) could be discarded. It should be noted that the nonlinearity and non-uniqueness observed between the reconstructed and measured ECa data in Figure 10a may also stem from either a violation of the LIN condition or manufacturer-specific design features of the instrument. Further investigation into these potential factors is recommended.

In summary, the multi-elevation method based on the SVD is an effective method to verify the consistency of ECa data, and calibrate the inconsistent data using the correct data predicted by the remaining ECa data (collected by FDEM excluding the incorrect measurement configurations).

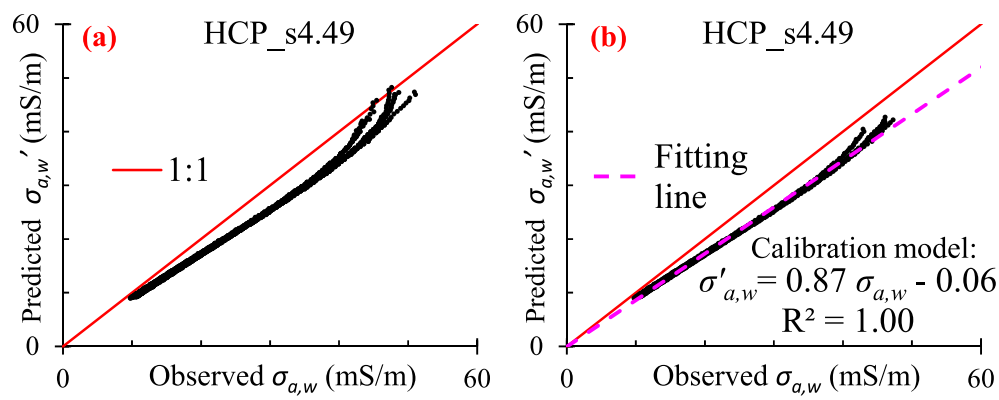

Figure 10. Calibration of ECa data from HCP_s4.49 using the predicted ECa values by Equation 10 at six sites: (a) raw data; (b) processed data after removing the ECa collected at probe heights lower than 0.5 m. The red line represents the 1:1 line.

4.2. Field Investigations Using Multi-Elevation UAV-FDEM Method

4.2.1. Investigation of Field Site 1: Riparian Transect

As shown in Figure 3, point measurements with multi –coil, -mode and –elevation configurations were conducted at the test sites in both summer and winter (red and green symbols, respectively). The EC values of soil profiles were inverted using a modified version of the FEMIC code (Elwaseif et al., 2017), where the original forward modeling module was replaced with the forward model code from FDEMtools3 (Deidda et al., 2023), and the algorithm was parallelized to enhance computational efficiency. Using the inversion results and spatial metadata (e.g., distance from the origin, altitude), the spatial distribution of EC along the flight route was generated via linear interpolation, as illustrated in Figures 11a and 11c.

These figures demonstrate significant variation in inverted EC values across test sites, reflecting the heterogeneous field environment where soil profiles are influenced by factors such as soil texture, groundwater level, land cover, and altitude. EC values generally increase with depth, likely due to rising soil moisture content. Notably, EC values at the base of profiles near the Yangtze River (sites S6 and W10) are lower than those at other sites. This anomaly may result from river water intrusion, as the EC of Yangtze River water (i.e., 25 and 35 mS/m in summer and winter, respectively) is markedly lower than that of the riparian unconfined aquifer.

In Figures 11a and 11c, the groundwater level line inferred from the single well (i.e., magenta line) is close to an EC contour line (i.e., black lines with values of 34 and 62 mS/m in summer and winter, respectively) in the relatively flat region, suggesting that EC values around the groundwater level are similar. However, these EC values around the groundwater table are clearly lower than those of the groundwater itself due to the insulating effect of soil particles. Specifically, solid soil particles with low conductivity (e.g., silicates) will impede the movement of ions in the soil solution, leading to a reduction in soil EC. The EC values near the groundwater table at sites away from the Yangtze River (i.e., S1 and W1) are significantly greater than those at other sites likely because of the effect of the high vegetation cover (e.g., weeds and trees, Figure 3), which may reduce soil water content in the unsaturated zone. The EC values of the shallow soil layer in Figure 11c (winter) are noticeably lower than those in Figure 11a (summer), which is consistent with the lower water table in winter and greater soil water depletion at shallow depths.

The UAV-FDEM in route measurement mode was employed to investigate the riparian transect in summer. The measurements were conducted at 44 heights ranging from 0.6 to 4.9 m for the HCP mode, and at the 22 heights ranging from 0.6 to 2.7 m for the VCP mode of CMD-Explorer. Notably, the ECa data collected by HCP_s4.49 were corrected using the linear calibration method (Figure 10). The EC values of soil profiles inverted by the modified FEMIC code using the ECa data collected by the multi-elevation UAV-FDEM are displayed in Figure 11b. This figure shows trends similar to the point model measurements in Figure 11a. However, compared to Figures 11a and 11b clearly exhibits higher-frequency variations. Hydrologically, the route mode does not provide more information than what can be obtained by interpolating the point mode, possibly because the hydrogeological conditions of the test site are relatively horizontally homogeneous.

For comparison, the ERT investigation results in winter along the survey line are shown in Figure 11d. This figure demonstrates a general increase in soil EC with depth, which is in line with the results of the multi-elevation UAV-FDEM (Figures 11a–11c). The anomalous high resistivity zone (see the long edges of the green dashed box) in the shallow soil layer, as measured by ERT, aligns with the low EC areas identified by the UAV-FDEM. Similarly, the anomalous low resistivity zone outlined by the green dashed box in the ERT image corresponds to slight increases in soil EC inferred from the UAV-FDEM measurements. However, compared to the multi-elevation UAV-FDEM, ERT provides a better representation of both lateral and vertical variations. This is primarily due to the dipole-dipole measurement configuration used for ERT, which is particularly sensitive to lateral variations in resistivity. Additionally, the UAV-FDEM measurements, especially at higher elevations, have a larger measurement footprint, leading to increased lateral smoothing of subsurface variations, which further contributes to the reduced resolution of lateral features compared to ERT.

In summary, the multi-elevation UAV-FDEM survey results show vertical variation in EC that is also revealed from the ERT survey. The UAV-FDEM surveys also show temporal changes in the vertical profile of EC that are consistent with groundwater level changes.

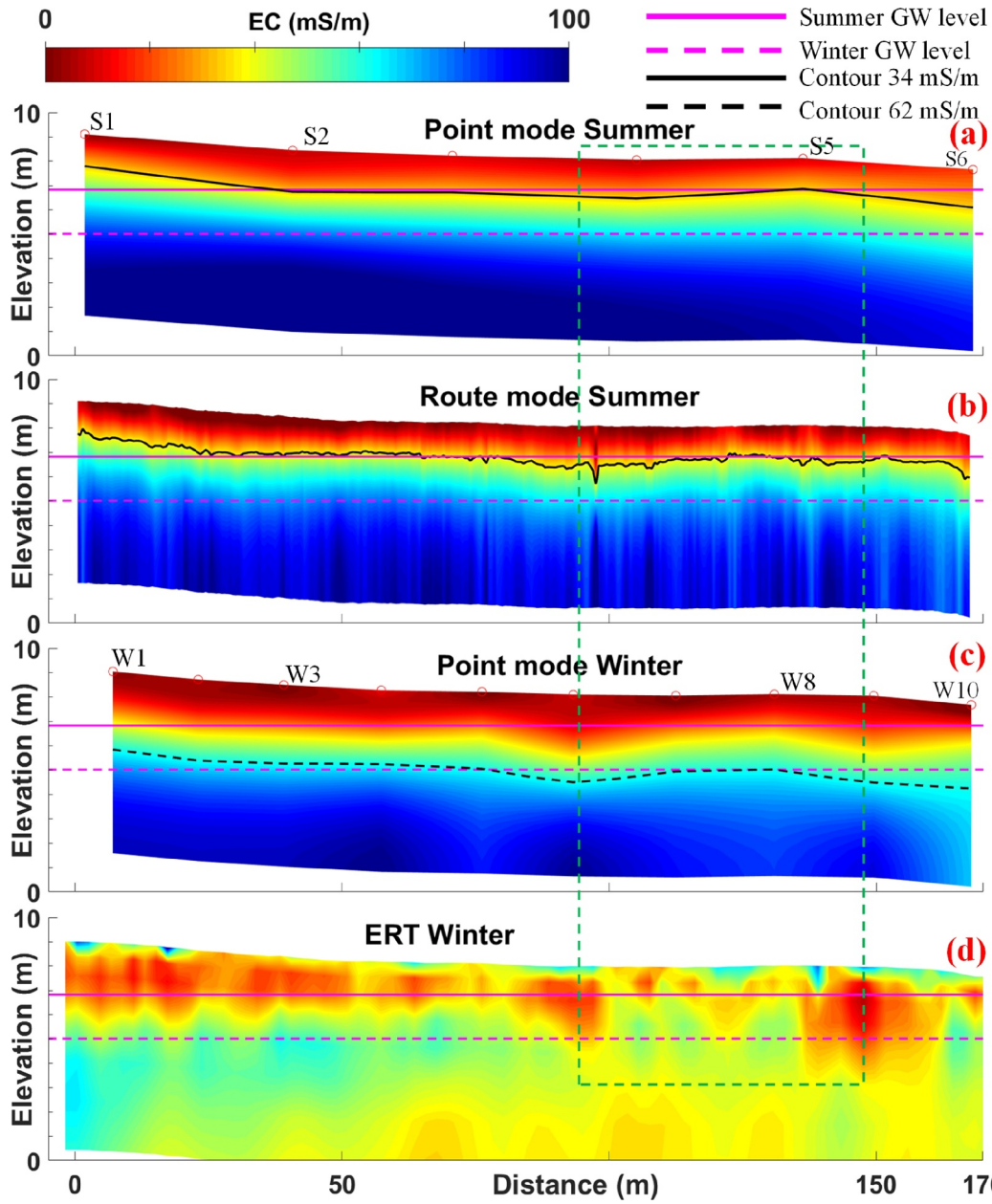

Figure 11. Geophysical inversion of FDEM with multi-configuration in the Riparian Transect: (a) point measurement mode in summer; (b) route measurement mode in summer; (c) point measurement mode in winter; (d) ERT survey results. The magenta solid and dash lines represent the groundwater level in summer and winter, respectively; the black solid and dash lines denote the EC contours of 34 and 62 mS/m, respectively; the red circles indicate the measurement points, and the green dash box highlights a high EC area.

4.2.2. Investigation of Field Site 2: Hot Spring Area

Based on the ECa data collected by the UAV-FDEM using a multi-configuration approach (including multi-coil, multi-mode, and multi-elevation) in the route measurement mode at the Hot Spring Area in Yangbajing, the EC values at the different depths (i.e., 1 ∼ 6 m) inverted by the modified FEMIC code are shown in Figure 12. This figure indicates that the EC values generally increase with the depth, as expected. Additionally, the EC values in the northwest area are significantly lower than those in the southeast area, which is in agreement with the ERT investigation results in Figure 5. In Figure 12, most springs are located within the high EC areas. The hot water upwelling throat (i.e., hot spring pathway) identified by the ERT survey (Figure 5) coincides with these high EC

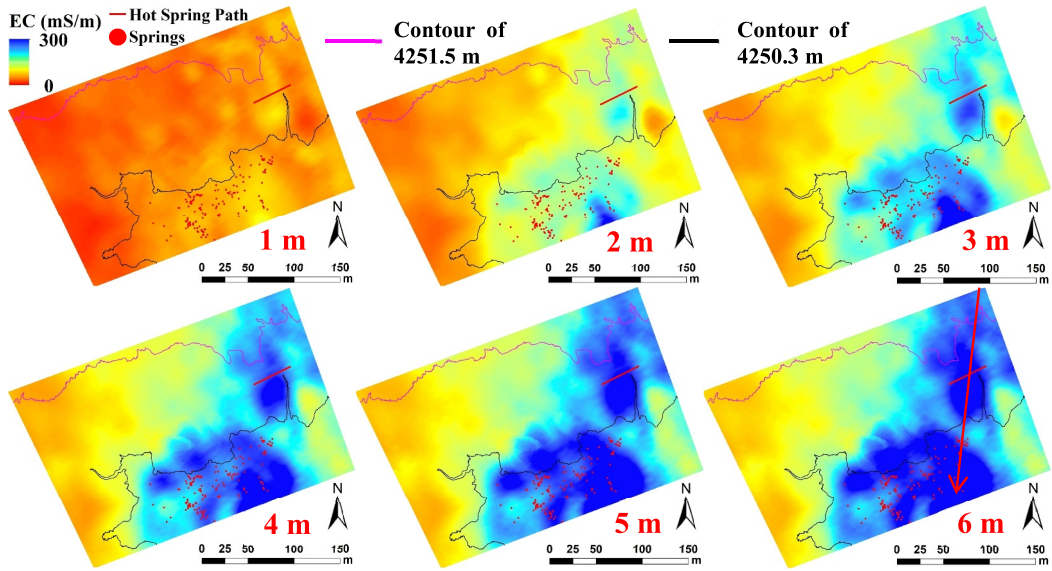

Figure 12. EC distribution at the different depths (i.e., 1–6 m) inverted by the modified FEMIC code using the ECa data collected by the multi-elevation UAV-FDEM method with the route measurement mode. The red arrow represents a possible undercurrent path of geothermal water, while the red line indicates the hot water upwelling pathway inferred from ERT investigation results (Figure 5). The red symbols denote the hot springs, and the magenta and black lines are the DSM contour lines of 4,251.5 and 4,250.3 m, respectively.

areas. Therefore, the high EC area measured by UAV-FDEM likely corresponds to the hot water intrusion zone. It is also suggested that there may be an undercurrent path of geothermal water flowing from northeast to southwest, as indicated by the red arrow in Figure 12.

In order to directly compare the UAV-FDEM results with the ERT results, the inverted EC values along the ERT survey line were extracted as shown in Figure 13. This figure demonstrates that the UAV-FDEM and ERT results are generally consistent. In particular, the hot water upwelling pathway inferred from the ERT survey corresponds with the high EC zone (Figure 13a). Therefore, the spatial EC distribution pattern measured by the multi-elevation

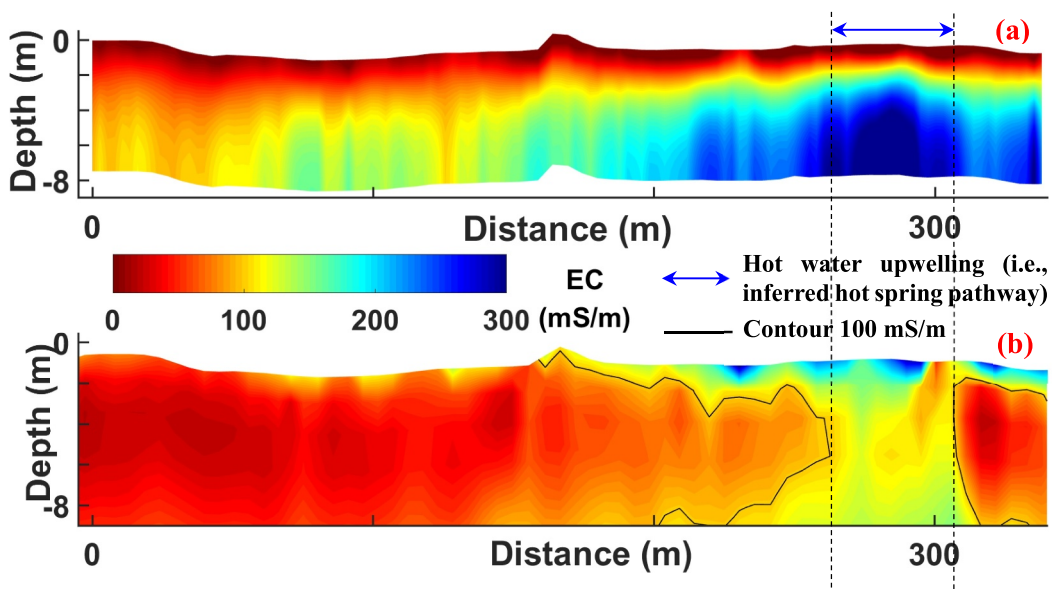

Figure 13. Comparison of the UAV-FDEM investigation results with the ERT results along the survey line: (a) UAV-FDEM and (b) ERT.

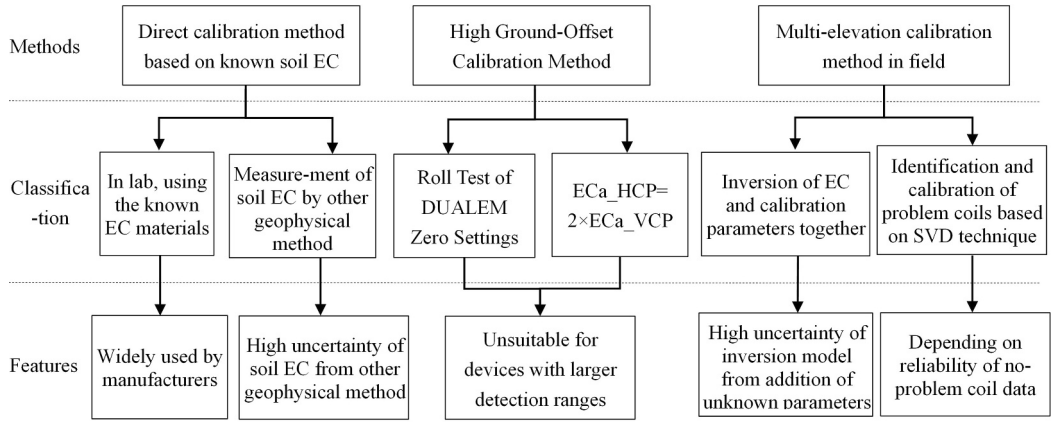

Figure 14. Features of widely used FDEM calibration methods in recent years.

UAV-FDEM method is similar to that investigated by the ERT method. However, the vertical EC variation in the UAV-FDEM results is more monotonic compared to the ERT results. This may be attributed to the greater depth of investigation of the ERT method compared to UAV-FDEM, as well as the lower resolution of the UAV-FDEM results. In other words, the footprint of FDEM measurements is larger than that of ERT. The consistently higher EC values obtained from UAV-FDEM surveys compared to ERT results may be attributed to the higher electromagnetic frequencies employed in FDEM systems relative to ERT. Note, however, that EM is, crudely speaking, a method for detecting conductors, not resistors, given the nature of signal generation. ERT, in comparison, is able to differentiate various levels of resistivity. These differences will inevitably lead to contrasts in derived EC models.

In summary, the multi-elevation UAV-FDEM results are consistent with an ERT survey along a transect, revealing a subsurface pathway of geothermal water. Furthermore, the efficiency of the measurement approach permitted a fully three-dimensional investigation of the area. This would not have been easily achievable with ERT.

5. Discussion

5.1. Necessities and Limitations of the Multi-Elevation Calibration Method

When FDEM methods are used to determine reliable estimate of the soil EC (through inversion), some form of calibration is necessary. FDEM calibration methods can be classified into three types (Figure 14): the direct method, the high ground-offset method and the multi-elevation method (Blanchy et al., 2020; McLachlan et al., 2021). For the direct method, the soil EC values should be known, which are typically measured in the laboratory or estimated by the geophysical exploration method (e.g., ERT) in field. The reliability of the direct method strongly depends on the EC measurement accuracy in the test area. For the high ground-offset method, it requires the instrument to be positioned above ground at a height greater than its detection depth (Abdu et al., 2007). However, this constraint is impractical for devices with larger detection ranges. For the multi-elevation calibration approach, previous studies have typically determined EC values and calibration model parameters together in an inverse model. This process can lead to high uncertainty because of ill-posedness and non-uniqueness problems (Minsley et al., 2014; Tan et al., 2019; Von Hebel et al., 2019). The new multi-elevation calibration approach introduced in this study employs the SVD technique to reconstruct observed ECa data, identify problematic Rx coils by comparison of the reconstructed and the observed ECa data, and calibrate the inconsistent measurements using the predicted data generated by ECa data from no-problem Rx coils (Figure 2). This novel approach eliminates the need for soil EC measurement and geophysical inversion, and, as shown, can be used successfully for calibrating multi-coil FDEM instruments (Figures 6–10). However, a direct comparison between inverted models using SVD calibration, uncalibrated data, or alternative calibration methods (e.g., large-offset calibration using drone data) was not performed in this study. Such comparisons would provide a more robust evaluation of the SVD method's performance relative to other approaches. Future work should include these comparative analyses to further validate the effectiveness of the SVD calibration method.

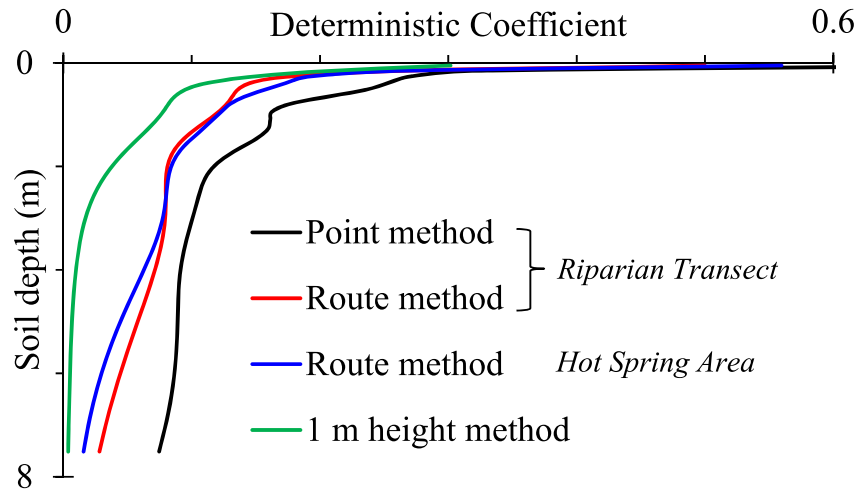

Figure 15. Deterministic coefficients of inverted EC values for different soil layers.

Additionally, because the forward model (Equation 2) is a linear system under the LIN condition, the system errors in FDEM observation data are challenging to calibrate using the new multi-elevation calibration approach. In other words, the new method only verifies the consistency of measurements collected by FDEM with different dipole center distances and coil orientations, but the accuracy of measurements still needs to be validated through the direct calibration method. Fortunately, FDEM manufacturers usually calibrate ECa for each Rx coil using the direct method before delivery (McLachlan et al., 2021). Therefore, the multi-elevation method plays a valuable role in FDEM instrument calibration by verifying the consistency of ECa data across different Rx coils.

5.2. Evaluating Performance and Survey Design

The single-elevation FDEM method is widely employed in field investigations. However, the value of using a multi-elevation approach over a single elevation includes several key benefits: enhanced sensitivity, improved accuracy, and robust data validation. A number of aspects discussed below may allow the operator to assess performance of the method compared to the conventional single-elevation approach, and also develop appropriate survey designs.

5.2.1. Resolution in Data Inversion

The resolution matrix in geophysical inversion is a widely used mathematical tool to evaluate the quality and reliability of estimated model parameters. It provides a measure of how well the inversion process can resolve or recover true model parameters from the observed data. The resolution matrix helps us understand how much influence the data has on the estimated model, revealing which parameters are well-determined and which ones are poorly constrained or influenced by noise. A regularized resolution matrix is defined as (Ren & Kalscheuer, 2020):

$$\boldsymbol{R} = \left(\boldsymbol{J}^T \boldsymbol{W}_d^T \boldsymbol{W}_d \boldsymbol{J} + \alpha \boldsymbol{W}_m^T \boldsymbol{W}_m\right)^{-1} \boldsymbol{J}^T \boldsymbol{W}_d^T \boldsymbol{W}_d \boldsymbol{J}\,. \tag{13}$$

where $\boldsymbol{J}$ is the Jacobian (or sensitivity) matrix, that is, the matrix of $\boldsymbol{A}$ in Equation 4 for the FDEM forward model; $\boldsymbol{W}_d$ and $\boldsymbol{W}_m$ are the weight matrix for data misfits and penalty terms, respectively, which are set as an identity matrix in this study; α is a regularization coefficient.

The diagonal elements of the resolution matrix $\boldsymbol{R}$ (Equation 13) indicate how closely the estimated parameter matches the true value, which are treated as the deterministic coefficients for the inverted EC values of different layers in a model. A value close to 1 on the diagonal suggests that the parameter is well resolved, while a value near 0 means that the data provide little information about that parameter. It can help us understand how well the inversion can distinguish EC at different depths. In shallow regions, where the observed data coverage is dense, the deterministic coefficient values are typically high. Conversely, in deeper regions with sparse observed data,

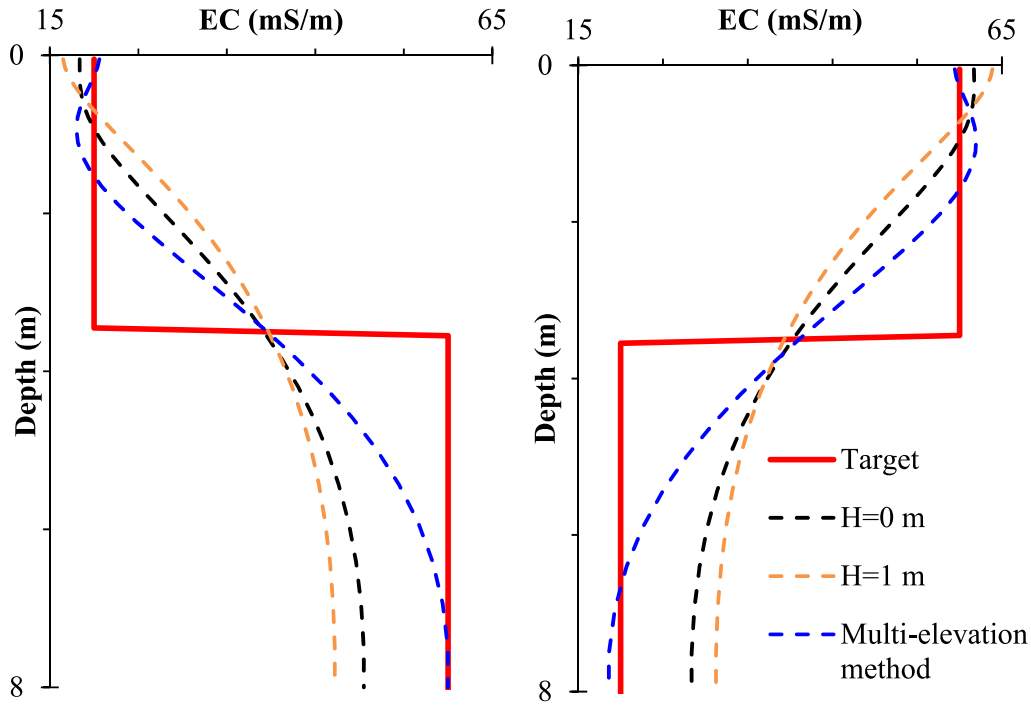

Figure 16. Inverted EC distribution in the soil profile using the synthetic data at different measurement heights.

the deterministic coefficient values tend to be low, indicating that the EC values at greater depths are poorly constrained.

The deterministic coefficients versus depth for multi-elevation and single-elevation measurement methods in this study are shown in Figure 15. This figure presents such analysis for all methods. The deterministic coefficient for different layers obviously decreases with depth, indicating that the quality and reliability of the estimated EC values diminish as depth increases. Furthermore, the deterministic coefficients of the single elevation measurement method (i.e., "1 m height method") recommended by manufacturers (for the three-coil instrument used here) are clearly lower than those of the multi-elevation method in each layer. This suggests that the uncertainty of the inversion model for the single-elevation measurement method is significantly greater than that for the multi-elevation method.

Figure 15 shows that the deterministic coefficients for different layers generally increase with the number of investigation probe heights. In the shallow soil layer, the deterministic coefficients of the multi-elevation route measurement method in the hot spring area are slightly greater than those in the riparian transect, possibly because a survey height (i.e., 0.4 m) for the HCP mode in the hot spring area is lower than that in the riparian transect. This suggests that a lower survey height in UAV-FDEM measurements can provide more effective information for geophysical inversion than a higher survey height. However, the selection of the minimum survey height will ultimately depend on the practical constraints of UAV-FDEM flights in the study area.

5.2.2. Accuracy of the Inversion

An approximate sensitivity matrix ($\boldsymbol{A}$) with five singular values (Equation 6) is sufficient to reconstruct the observed ECa. In other words, the FDEM forward model (Equation 2) may only possess five degrees of freedom. The FDEM instrument used in this study, employing the single elevation method, can provide six ECa values from three Rx coils in both HCP and VCP modes (although the two measurement triplets need to be collected separately as the instrument must be rotated between VCP and HCP modes). Generally, using these six observed data, it is, in theory, possible to estimate six unknown parameters. Therefore, the inversion results from the single elevation method may be comparable to those from multi-elevation methods.

Table 1
Optimization Results of Probe Heights for Different Number of Survey Elevations

	No.	Best mean of deterministic coefficients	The best combination of probe heights (m) for different number of survey elevations				
Number of heights	1	0.279	0				
	2	0.333	0	7			
	3	0.352	0	0.15	7		
	4	0.361	0	0.15	0.2	7	
	5	0.368	0	0.05	0.15	0.2	7
	141/ALL	0.420					

In order to evaluate the reliability of the multi-elevation method, an ideal semi-infinite stratum model was constructed, consisting of 80 soil layers, each with a thickness of 0.1 m. Two types of EC distributions in the soil profile were considered. In one case (Figure 16a), we assume that EC value is 20 mS/m in the shallow soil layer (i.e., from 0 to 3.5 m in depth), while it is 60 mS/m in the deeper layer (i.e., below 3.5 m). In contrast, in the other case (Figure 16b), the EC values are 60 mS/m in the shallow soil layer and 20 mS/m in the deep layer. Based on these ideal models, we first employed the forward model to generate the ECa data collected by CMD-Explorer within a probe height range of 0–7 m at an interval of 0.05 m. Next, we separately used ground-level (0 m), 1 m, and all (i.e., multi-elevation) synthetic ECa data to estimate the EC distribution in the soil profile using the modified FEMIC code. The inversion results are shown in Figure 16.

Figure 16 shows that using the single elevation measurements, the estimated EC values can generally capture the trend of assumed (i.e., target) EC values. This supports our earlier findings: the single elevation measurements with six ECa values can be used for FDEM geophysical inversion. However, the inversion results using the multi-elevation measurements match the target values much better than those using the single elevation method, as shown in Figure 16. In other words, the multi-elevation measurement method obviously improves the accuracy of FDEM investigations. In Figure 16, the inverted EC values from ground-level (i.e., 0 m elevation) measurements are slightly better than those from 1 m elevation measurements. This also confirmed our earlier findings: the low height survey results provide more effective information than the high height investigations. The over-smoothing of the inversion results (Figure 16, and examples shown in the three case studies earlier) may be related to the inversion algorithm implemented in the FEMIC code used in our study. In future work, we plan to explore alternative open-source codes such as EMagPy (McLachlan et al., 2021) and FDEMtools (Buccini et al., 2024) to potentially enhance the resolution of the inverse models, for example, by adopting different regularization operators in the inversion.

5.2.3. Optimal Combination of Survey Heights

In the route measurement mode of the multi-elevation UAV-FDEM method, it can be challenging to collect ECa data at all probe heights. Thus, it is worthwhile considering the optimization of measurement heights. Based on the ideal semi-infinite stratum model described in Section 2.3, we generated all possible probe height combinations for the different number of survey elevations, and then calculated the deterministic coefficients in the soil profile using Equation 13. Next, we used the mean of deterministic coefficients (Equation 13) in the soil profile as the optimal objective, and determined the best probe height combination by comparing the objective values across all combinations. The optimization results are shown in Table 1. This table indicates that the mean of deterministic coefficients in the soil profile increases with the number of measurement elevations used. This finding suggests that the more multi-elevation measurements taken, the more accurate the inversion results will be, as expected.

The best combination of probe heights in Table 1 shows that the ground-level (i.e., 0 m elevation) measurements provide more effective information than measurements taken at other elevations. Compared to the high elevation measurements, the lower elevation measurements (such as 0.05, 0.15 and 0.2 m probe heights) provide more effective information. However, the high elevation measurements (e.g., 7 m probe height) show a noticeable improvement in the deterministic coefficient, and should not be excluded from the multi-elevation measurements.

It is clear that low and high elevations add much information. The analysis above shows how the operator may decide to optimize the selection of measurement heights, subject to logical constraints.

6. Conclusion

FDEM is an efficient tool for investigating the EC distribution over relatively shallow depths in the field, and has been used for numerous applications related to groundwater resource management. However, the traditional handheld method recommended by manufacturers does not, in our opinion, take full advantage of non-invasive detection offered by FDEM devices. In this study, a UAV airborne FDEM (UAV-FDEM) approach is proposed, which can carry a FDEM probe to conduct investigations in field at specific flight heights along a planned route. Based on the UAV-FDEM system, a multi-elevation calibration method has been developed, allowing the verification of the consistency of ECa collected by different FDEM coils and the subsequent calibration of inconsistent data. Although the new method cannot directly check the accuracy of FDEM measurements, it is a favorable supplement for testing the reliability of measurement data. The new multi-elevation calibration method had been successfully used to correct ECa data collected by CMD-Mini-Explorer and CMD-Explorer in this study.

In order to test and demonstrate the proposed UAV-FDEM method, we employed it to investigate a riparian zone of the Yangtze River and a hot spring area using multi-elevation measurements. The survey results show that the UAV-FDEM survey results are comparable to those obtained from ERT. The EC anomalous zones detected by UAV-FDEM are in agreement with those detected by ERT. The UAV-FDEM surveys detected temporal changes in soil EC that correspond with observed groundwater level changes at the riparian zones study site. In a second study, the surveys successfully delineated the intrusion area and subsurface path of geothermal water. In comparison to conventional ground-based single-elevation measurements, the multi-elevation UAV-FDEM method clearly improves the deterministic coefficients for the inverted EC value of different soil layers, and reduces the uncertainty of the geophysical inversion results.

For efficient deployment of the method, the operator should assess the optimum set of measurement heights prior to conducting field measurements. Such a set should cover a wide range of heights to enhance reliability of the subsequent data inversion. At the same time, attention should be paid to the signal-to-noise ratio, as excessively high FDEM survey heights may reduce the instrument's detection accuracy and affect the survey results.

Although conventional handheld, ground-based, FDEM surveys are likely to remain popular, we believe that UAV-based measurements using FDEM instruments can offer immense value for surveying relatively large areas efficiently and will prove effective for deployment in areas where ground-based access is restricted, impractical or unsafe. For example, application of conventional approaches over wetlands or surface water bodies can be challenging, but are ideally suited to UAV-based surveys. As UAV technology evolves, we anticipate much more widespread use to assist in near surface geophysical investigations.

Future research will prioritize validating the UAV-FDEM method across diverse hydrogeological settings, including fractured bedrock and coastal aquifers, to refine its scalability and robustness. Advancements in machine learning-driven inversion algorithms could further enhance resolution in heterogeneous environments. Additionally, coupling UAV-FDEM with satellite-based hydrologic models may enable real-time groundwater monitoring at much larger scales. Addressing cost-effectiveness and regulatory barriers for widespread deployment in low-resource regions will also be critical. By bridging gaps between geophysical innovation and practical water management needs, this methodology holds promise for transforming high-resolution groundwater mapping into a routine tool for sustainable resource governance, for example, under climate change.

Conflict of Interest

The authors declare no conflicts of interest relevant to this study.

Data Availability Statement

The data used in this paper is accessible at (Cheng, 2025).

Acknowledgments
This research was funded by the National Key Research and Development Program of China (Grant No. 2022YFC3202301), the Key Technologies Research on Development and Service of Yellow River Simulator for Super-Computing Platform (Grant No. 201400210900), YRCC Outstanding Young Talents Sci-Tech Project (Grant No. HQK-202304), the Second Tibetan Plateau Scientific Expedition and Research Program (STEP; Ministry of Science and Technology, MOST; Grant No. 2019QZKK0207-02), and the National Natural Science Foundation of China (Grant No. 42030506, U21A2004, 52179013, and 42071039). We are grateful to the Associate Editor and three anonymous reviewers for their constructive comments on an earlier version of the manuscript.

References

Abdu, H., Robinson, D., & Jones, S. (2007). Comparing bulk soil electrical conductivity determination using the DUALEM-1S and EM38-DD electromagnetic induction instruments. *Soil Science Society of America Journal*, *71*(1), 189–196. https://doi.org/10.2136/sssaj2005.0394

Andrade, F. C. M. D., & Fischer, T. (2018). Generalised relative and cumulative response functions for electromagnetic induction conductivity meters operating at low induction numbers. *Geophysical Prospecting*, *66*(3), 595–602.

Binley, A., Hubbard, S. S., Huisman, J. A., Revil, A., Robinson, D. A., Singha, K., & Slater, L. D. (2015). The emergence of hydrogeophysics for improved understanding of subsurface processes over multiple scales. *Water Resources Research*, *51*(6), 3837–3866. https://doi.org/10.1002/2015wr017016

Binley, A., & Slater, L. (2020). *Resistivity and induced polarization: Theory and applications to the near-surface Earth*. Cambridge University Press.

Bjerg, T., Lima Simões da Silva, E., & Døssing, A. (2020). Investigation of UAV noise reduction for electromagnetic induction surveying. In *Paper presented at NSG2020 3rd Conference on geophysics for mineral exploration and mining*. European Association of Geoscientists & Engineers.

Blanchy, G., Watts, C. W., Richards, J., Bussell, J., Huntenburg, K., Sparkes, D. L., et al. (2020). Time-lapse geophysical assessment of agricultural practices on soil moisture dynamics. *Vadose Zone Journal*, *19*(1), e20080. https://doi.org/10.1002/vzj2.20080

Boaga, J. (2017). The use of FDEM in hydrogeophysics: A review. *Journal of Applied Geophysics*, *139*, 36–46. https://doi.org/10.1016/j.jappgeo.2017.02.011

Buccini, A., de Alba, P. D., & Pes, F. (2024). An alternating direction multiplier method for the inversion of FDEM data. *Journal of Scientific Computing*, *101*(1), 14. https://doi.org/10.1007/s10915-024-02652-9

Cheng, Q. (2025). Original data and code for "UAV-FDEM method" [Dataset]. *Figshare*. https://doi.org/10.6084/m9.figshare.28815077

Deidda, G. P., Díaz de Alba, P., Pes, F., & Rodriguez, G. (2023). Forward electromagnetic induction modelling in a multilayered half-space: An open-source software tool. *Remote Sensing*, *15*(7), 1772. https://doi.org/10.3390/rs15071772

Delefortrie, S., De Smedt, P., Saey, T., Van De Vijver, E., & Van Meirvenne, M. (2014). An efficient calibration procedure for correction of drift in EMI survey data. *Journal of Applied Geophysics*, *110*, 115–125. https://doi.org/10.1016/j.jappgeo.2014.09.004

Delefortrie, S., Saey, T., De Pue, J., Van De Vijver, E., De Smedt, P., & Van Meirvenne, M. (2016). Evaluating corrections for a horizontal offset between sensor and position data for surveys on land. *Precision Agriculture*, *17*(3), 349–364. https://doi.org/10.1007/s11119-015-9423-8

De Smedt, P., Delefortrie, S., & Wyffels, F. (2016). Identifying and removing micro-drift in ground-based electromagnetic induction data. *Journal of Applied Geophysics*, *131*, 14–22. https://doi.org/10.1016/j.jappgeo.2016.05.004

Doolittle, J. A., & Brevik, E. C. (2014). The use of electromagnetic induction techniques in soils studies. *Geoderma*, *223*, 33–45. https://doi.org/10.1016/j.geoderma.2014.01.027

Elwaseif, M., Robinson, J., Day-Lewis, F., Ntarlagiannis, D., Slater, L., Lane, J., et al. (2017). A matlab-based Frequency-Domain Electromagnetic Inversion Code (FEMIC) with graphical user interface. *Computers Geosciences-UK*, *99*, 61–71. https://doi.org/10.1016/j.cageo.2016.08.016

Guo, Q., Wang, Y., & Liu, W. (2007). Major hydrogeochemical processes in the two reservoirs of the Yangbajing geothermal field, Tibet, China. *Journal of Volcanology and Geothermal Research*, *166*(3–4), 255–268. https://doi.org/10.1016/j.jvolgeores.2007.08.004

Hanssens, D., Delefortrie, S., De Pue, J., Van Meirvenne, M., & De Smedt, P. (2019). Frequency-domain electromagnetic forward and sensitivity modeling: Practical aspects of modeling a magnetic dipole in a multilayered half-space. *IEEE Geoscience and Remote Sensing Magazine*, *7*(1), 74–85. https://doi.org/10.1109/mgrs.2018.2881767

Heil, K., & Schmidhalter, U. (2019). Theory and guidelines for the application of the geophysical sensor EM38. *Sensors*, *19*(19), 4293. https://doi.org/10.3390/s19194293

Huang, X., Liu, Y., & Cai, J. (2014). Footprint for frequency-domain airborne electromagnetic systems. *Geophysics*, *79*(6), E243–E254. https://doi.org/10.1190/geo2014-0007.1

Kamenetsky, F., & Oelsner, C. (2000). Distortions of EM transients in coincident loops at short time-delays. *Geophysical Prospecting*, *48*(6), 983–993. https://doi.org/10.1046/j.1365-2478.2000.00228.x

Karaoulis, M., Ritsema, I., Bremmer, C., & De Kleine, M. (2020). Drone-Borne Electromagnetic (DREM) surveying in the Netherlands. In *Paper presented at NSG2020 26th European meeting of environmental and engineering geophysics*. European Association of Geoscientists & Engineers.

Karaoulis, M., Ritsema, I., Bremmer, C., De Kleine, M., Oude Essink, G., & Ahlrichs, E. (2022). Drone-Borne Electromagnetic (DR-EM) surveying in the Netherlands: Lab and field validation results. *Remote Sensing*, *14*(21), 5335. https://doi.org/10.3390/rs14215335

Lavoué, F., van der Krak, J., Rings, J., André, F., Moghadas, D., Huisman, J., et al. (2010). Electromagnetic induction calibration using apparent electrical conductivity modelling based on electrical resistivity tomography. *Near Surface Geophysics*, *8*(6), 553–561. https://doi.org/10.3997/1873-0604.2010037

Lin, J., Kang, L., Liu, C., Ren, T., Zhou, H., Yao, Y., et al. (2019). The frequency-domain airborne electromagnetic method with a grounded electrical source. *Geophysics*, *84*(4), E269–E280. https://doi.org/10.1190/geo2017-0777.1

McLachlan, P., Blanchy, G., & Binley, A. (2021). EMagPy: Open-source standalone software for processing, forward modeling and inversion of electromagnetic induction data. *COMPUT GEOSCI-UK*, *146*, 104561. https://doi.org/10.1016/j.cageo.2020.104561

McNeill, J. D. (1980). *Electromagnetic terrain conductivity measurement at low induction numbers*. Geonics Ltd. Technical Note TN-6.

Minsley, B. J., Abraham, J. D., Smith, B. D., Cannia, J. C., Voss, C. I., Jorgenson, M. T., et al. (2012). Airborne electromagnetic imaging of discontinuous permafrost. *Geophysical Research Letters*, *39*(2). https://doi.org/10.1029/2011gl050079

Minsley, B. J., Kass, M. A., Hodges, G., & Smith, B. D. (2014). Multielevation calibration of frequency-domain electromagnetic data. *Geophysics*, *79*(5), E201–E216. https://doi.org/10.1190/geo2013-0320.1

Mitsuhata, Y., Ueda, T., Kamimura, A., Kato, S., Takeuchi, A., Aduma, C., & Yokota, T. (2022). Development of a drone borne electromagnetic survey system for searching for buried vehicles and soil resistivity mapping. *Near Surface Geophysics*, *20*(1), 16–29. https://doi.org/10.1002/nsg.12189

Ralchenko, M., Samson, C., Holladay, S., & Polowick, C. (2018). Towards an unmanned airborne platform for electromagnetic geophysical surveying. In *Paper presented at 2018 SEG International exposition and annual meeting*.

Ren, Z., & Kalscheuer, T. (2020). Uncertainty and resolution analysis of 2D and 3D inversion models computed from geophysical electromagnetic data. *Surveys in Geophysics*, *41*(1), 47–112. https://doi.org/10.1007/s10712-019-09567-3

Robinson, D. A., Binley, A., Crook, N., Day-Lewis, F. D., Ferré, T. P. A., Grauch, V. J. S., et al. (2008). Advancing process-based watershed hydrological research using near-surface geophysics: A vision for, and review of, electrical and magnetic geophysical methods. *Hydrological Processes: International Journal*, *22*(18), 3604–3635. https://doi.org/10.1002/hyp.6963

Rubin, Y., & Hubbard, S. S. (2006). *Hydrogeophysics*. Springer Science & Business Media.

Saksa, P. J., & Sorsa, J. (2017). System stability and calibrations for hand-held electromagnetic frequency domain instruments. *Journal of Applied Geophysics*, *140*, 84–92. https://doi.org/10.1016/j.jappgeo.2017.03.010

Selepeng, A. T. (2016). *Three dimensional numerical modeling of loop-loop electromagnetic data at low induction numbers*. Akita University.

Siemon, B., Christiansen, A. V., & Auken, E. (2009). A review of helicopter-borne electromagnetic methods for groundwater exploration. *Near Surface Geophysics*, *7*(5–6), 629–646. https://doi.org/10.3997/1873-0604.2009043

Stewart, G. W. (1993). On the early history of the singular value decomposition. *SIAM Review*, *35*(4), 551–566. https://doi.org/10.1137/1035134

Tan, X., Mester, A., von Hebel, C., Zimmermann, E., Vereecken, H., van Waasen, S., & van der Kruk, J. (2019). Simultaneous calibration and inversion algorithm for multiconfiguration electromagnetic induction data acquired at multiple elevations. *Geophysics*, *84*(1), EN1–EN14. https://doi.org/10.1190/geo2018-0264.1

Vélez-Nicolás, M., García-López, S., Barbero, L., Ruiz-Ortiz, V., & Sánchez-Bellón, Á. (2021). Applications of Unmanned Aerial Systems (UASs) in hydrology: A review. *Remote Sens-Basel*, *13*(7), 1359. https://doi.org/10.3390/rs13071359

Vilhelmsen, T. B., Grayver, A. V., & Døssing, A. (2024). Drone-towed electromagnetic and magnetic systems for subsurface characterization and archaeological prospecting. *Near Surface Geophysics*, *22*(6), 617–635. https://doi.org/10.1002/nsg.12320

Von Hebel, C., van der Kruk, J., Huisman, J. A., Mester, A., Altdorff, D., Endres, A. L., et al. (2019). Calibration, conversion, and quantitative multi-layer inversion of multi-coil rigid-boom electromagnetic induction data. *SENSORS-BASEL*, *19*(21), 4753. https://doi.org/10.3390/s19214753

Walter, C., Braun, A., & Fotopoulos, G. (2021). Characterizing electromagnetic interference signals for unmanned aerial vehicle geophysical surveys. *Geophysics*, *86*(6), J21–J32. https://doi.org/10.1190/geo2020-0895.1

Ward, S. H., & Hohmann, G. W. (1988). Electromagnetic theory for geophysical applications. In M. N. Nabighian (Ed.), *Electromagnetic methods in applied geophysics: Volume 1, theory* (pp. 131–311). Society of Exploration Geophysicists.